Title

Yeast PRPP amidotransferase assembles into fine granules to promote *de novo* purine synthesis through intermolecular substrate channeling

Masak Takaine[1,2], Rikuri Morita[3]

[1]GIAR and [2]IMCR, Gunma University, Maebashi, Japan; [3]Center for Computational Sciences, University of Tsukuba, Ibaraki, Japan

Keywords: purine biosynthesis, *de novo* purine synthesis, PRPP amidotransferase (PPAT), Ade4, yeast

*Correspondence should be addressed to: masaktakaine@gunma-u.ac.jp (M.T.)

Highlights

- Budding yeast PRPP amidotransferase (PPAT) forms intracellular dynamic granules in response to the deprivation of environmental purine bases.
- The assembly of PPAT granules is driven by ribosome crowding in the cytoplasm induced by TORC1.
- Pure PPAT proteins condensate into granule-sized particles *in vitro* under molecular crowding conditions.
- The interaction of PPAT with purine nucleotides prevents granule assembly.
- The condensation of PPAT in granules permits the intermolecular channeling of intermediates, thereby facilitating *de novo* purine synthesis.

Summary

De novo purine synthesis (DPS) is up-regulated under conditions of high purine demands to ensure the mass production of genetic materials and chemical energy, thereby supporting cell proliferation. However, the mechanisms by which DPS is activated remain unclear. We herein demonstrated that PRPP amidotransferase (PPAT), the rate-limiting enzyme in DPS, condensated into granules in *Saccharomyces cerevisiae* cells under purine-depleted conditions. The assembly of granules required phase separation driven by target of rapamycin complex 1 (TORC1)-induced ribosome biosynthesis. A biochemical analysis revealed that the self-assembly of PPAT molecules accounted for granule formation and submillimolar levels of purine nucleotides inhibit self-assembly. Cells unable to form PPAT granules showed growth defects, indicating the physiological importance of granules for the promotion of DPS. These results suggest that the condensation of PPAT by phase transition is a mechanism that regulates DPS sensitively responding to both TORC1 activity and cellular purine demands.

Introduction

Purine nucleotides and their derivatives are involved in many cellular processes and, thus, are essential metabolites for every living organism. The purine nucleotide triphosphates ATP and GTP serve as the energy currencies of cells. Purine metabolites are also incorporated into genetic material, namely, DNA and RNA, as well as coenzymes, such as NAD and coenzyme A. Purine nucleotides are synthesized via both salvage and *de novo* pathways. In mammalian cells, as long as extracellular purine bases are available, purine nucleotides are preferentially synthesized from the recycling of bases through the salvage pathway[1]. Under the condition of a high purine demand (*e.g.*, in actively proliferating cells), the *de novo* pathway is activated to supply higher levels of purine nucleotides[1]. Disorders in the regulation of purine metabolism are associated with various diseases, such as cancer, hyperuricemia (gout), and immunological defects [2, 3]. A more detailed understanding of the regulatory mechanisms underlying purine metabolism will provide insights into the molecular basis of these diseases and facilitate the identification of their therapeutic targets.

The *de novo* purine biosynthetic pathway comprises ten highly conserved sequential chemical reactions that are performed by six enzymes and transforms phosphoribosyl pyrophosphate (PRPP) into inosine 5′-monophosphate (IMP). IMP is subsequently converted into adenosine 5′-monophosphate (AMP) or guanine 5′-monophosphate (GMP) via two branched paths (Fig. 1H). Among these enzymes, only the activity of PRPP amidotransferase (PPAT) (EC 2.4.2.14) is regulated by purine nucleotides [4]. Therefore, PPAT is presumed to be the rate-limiting enzyme in the pathway and plays an important role in the regulation of *de novo* purine synthesis. PPAT catalyzes the first step of the *de novo* pathway, namely, the transfer of amino groups from glutamine onto PRPP to produce 5-phosphoribosylamine (PRA) (eq. 1). This reaction is further divided into two half-reactions: the deprivation of ammonia (NH_3) from glutamine (eq. 2) and the ligation of NH_3 with PRPP (eq. 3). PPAT is a bifunctional enzyme with two catalytic domains: an N-terminal glutamine amidotransferase (GATase) domain that catalyzes the former reaction and a C-terminal phosphoribosyltransferase (PRTase) domain that catalyzes the latter reaction.

$$\mathbf{PRPP + glutamine + H_2O \rightarrow PRA + glutamate + PP_i} \quad \text{(eq. 1)}$$

$$\mathbf{glutamine + H_2O \rightarrow NH_3 + glutamate} \quad \text{(eq. 2)}$$

$$\mathbf{PRPP + NH_3 \rightarrow PRA + PP_i} \quad \text{(eq. 3)}$$

The enzymatic properties and catalytic mechanisms of PPAT have been extensively investigated for decades mainly using enzymes purified from *Escherichia coli* [5] and *Bacillus subtilis* [6]. One of the important features of this enzyme is feedback inhibition by the end-products of the *de novo* pathway, such as AMP and GMP [5-7]. The feedback inhibition of PPAT has been implicated in the suppression of *de novo* purine synthesis in the presence of extracellular salvageable purine bases (and its activation in purine starvation) in mammalian culture cells [7]. Moreover, in the budding yeast *Saccharomyces cerevisiae* and filamentous fungus *Ashbya gossypii*, the expression of PPAT is repressed by the presence of extracellular purine bases [8, 9].

Although the feedback inhibition of PPAT by purine nucleotides appears to play a pivotal role in the regulation of purine synthesis, millimolar levels of AMP or GMP are required for the inhibition of PPAT activity[5, 7, 9]. Intracellular concentrations of AMP and GMP are estimated to be 40–80 and 10–20 μM, respectively, in yeast or mammalian cells under nutrient-rich conditions[10]. The 10- to 100-fold difference between physiological and inhibitory concentrations of AMP and GMP raises the question whether the feedback inhibition of PPAT is directly relevant to the regulation of purine synthesis *in vivo*. Other layers of regulation of PPAT activity, such as post-translational modifications and intracellular signaling, may be involved; however, this has not yet been investigated.

A growing body of evidence reveals that many metabolic enzymes form condensates in cells in response to external stimuli in order to regulate cellular metabolism [11]. For example, the pyruvate kinase Cdc19 in budding yeast reversibly aggregates into large foci upon glucose starvation and heat shock [12, 13]. The assembly of foci protects Cdc19 from stress-induced degradation and inactivates the enzyme, both of which are important for the efficient formation of stress granules and the regrowth of cells after stress relief. Cytidine triphosphate synthase (CTPS) forms filamentous structures in bacteria, yeast, human, and fly germline cells [14-17]. Bacterial CTPS polymerizes into filaments corresponding to the inactive state of the enzyme, while the polymerization of human CTPS into filaments activates the enzyme [18, 19]. PPAT also reversibly localizes to cytoplasmic condensates upon the depletion of extracellular purine bases in budding yeast and HeLa cells [20, 21]. In the case of HeLa cells, PPAT colocalizes with five other enzymes involved in *de novo* purine synthesis in condensates. This multi-enzyme cellular complex is called a purinosome. The molecular basis that regulates the assembly of these PPAT condensates and the physiological importance of the condensates remain unclear.

111 We herein demonstrated that PPAT formed dynamic intracellular granules through phase
112 separation in budding yeast cells in the absence of external purine bases. Active ribosome
113 synthesis promoted by target of rapamycin complex 1 (TORC1) is essential for the
114 molecular crowding of the cytoplasm harnessed to drive phase transition. A biochemical
115 analysis demonstrated that PPAT by itself was sufficient for the assembly of granules, and
116 purine nucleotides at submillimolar concentrations may suppress their assembly.
117 Furthermore, we found that the formation of PPAT granules was important for *de novo*
118 purine synthesis to promote cell proliferation under purine-depleted conditions.
119 Consistent with this result, a computer simulation supported the possible condensation-
120 dependent activation of the enzyme. Collectively, the present results suggest that the
121 condensation of PPAT by phase transition is a mechanism that quickly regulates purine
122 synthesis in response to both TORC1 activity and the concentrations of purine nucleotides.

Results

The yeast phosphoribosylpyrophosphate amidotransferase Ade4 concentrates in fine granules

We visualized the localization of the Ade4 protein, the yeast PPAT, by C-terminally tagging the chromosomal *ADE4* gene with a single yeast codon-optimized GFP (hereafter referred to as GFP). As demonstrated in previous studies [20, 22], Ade4-GFP showed a large focus in cells transferred into medium lacking purine bases, but not in the presence of purine bases (Figs. 1A and 1S1A). However, Ade4-mGFP, Ade4 tagged with a GFP bearing the monomeric mutation A206K[23], appeared as numerous fine dim dots under the same conditions. Ade4-monomeric NeonGreen (mNG) also formed fine granules, but with markedly higher fluorescence intensities (Fig. 1A-B). Moreover, Ade4 tagged with the monomeric red fluorescent protein mKate2 (Ade4-mKate2) showed similar granule localization (Fig. 1S1B). Therefore, we concluded that Ade4-GFP concentrated into 1-2 foci through the dimerization of the GFP moiety. In subsequent experiments, we mainly examined the granules of Ade4-mNG to elucidate the molecular mechanisms regulating the condensation of Ade4 molecules. In some cases, we examined the assembly of Ade4-GFP foci because they basically have the same properties as Ade4-mNG granules and are easily detectable under a microscope because they are brighter than granules and, thus, are suitable for high-content imaging. A close examination of Ade4-mNG granules revealed that they were highly motile and localized throughout the cytoplasm (Fig. 1C). Moreover, time-lapse imaging revealed that the granules were a dynamic structure: they assembled within 40 min after the depletion of an extracellular purine base (adenine) (Figs. 1D, F and 1S1C, and Movies S1-S3) and disassembled within 10 min after supplementation with adenine (Figs. 1E, G and 1S1D, and Movies S4-S6).

Ade4 granules have liquid-like properties

The reversible assembly and dynamic nature of Ade4-mNG granules prompted us to speculate that they are liquid-like assemblies rather than static, solid-like aggregates. Therefore, we treated cells having Ade4-mNG with the aliphatic alcohol 1,6-hexanediol, which is known to dissolve a range of intracellular membrane-less structures [24]. The permeabilization of yeast cells by digitonin did not affect the assembly of Ade4-mNG granules, whereas the granules significantly disassembled within 10 min when exposed to 10% 1,6-hexanediol plus digitonin, revealing their liquid-like properties (Fig. 2A-B).

Previous findings suggested the importance of an intrinsically disordered region (IDR) in

159 the formation of intracellular membrane-less structures[25]. Therefore, we examined the
160 amino acid sequences of Ade4 and other PPATs using the DISOPRED algorithm[26], which
161 predicts IDR using a neural network-based method. We identified an IDR at the C
162 terminus of Ade4 (Fig. 2C). The C-terminal IDR was highly conserved in Ade4
163 homologues of Ascomycota and whole fungi (Fig. 2S1). It was also conserved in the
164 PPATs of species in other kingdoms, particularly those in bacteria and mammals (Fig.
165 2S2). On the other hand, the amino acid sequences of IDRs vary across species, even in
166 yeasts (Fig. 2S3). A mNG-tagged Ade4 mutant lacking the IDR, Ade4ΔIDR-mNG, was
167 incapable of forming granule-like structures, suggesting that the IDR is required for the
168 assembly of Ade4 granules (Fig. 2D). Taken together, these results suggest that Ade4
169 molecules condensate into fine motile granules through IDR-dependent phase separation.
170

171 Formation of Ade4 granules requires active TORC1 and ribosome biogenesis

172 We examined the factors required for phase separation, which drives the assembly of
173 Ade4 granules. During the course of this study, TORC1 has been suggested to control
174 phase separation in the cytoplasm of yeast and mammalian cells by tuning ribosome
175 crowding[27]. Therefore, we investigated whether TORC1 plays a role in the formation of
176 Ade4 granules. In cells, rapamycin has been shown to bind to FKBP12, and this complex
177 potently inhibited TORC1[28]. The addition of rapamycin suppressed the assembly of
178 Ade4-GFP foci in wild-type cells, while rapamycin did not affect the foci in cells lacking
179 Fpr1 (budding yeast FKBP1) (Fig. 3A). Rapamycin also significantly suppressed the
180 assembly of Ade4-mNG granules in wild-type cells (Fig. 3B-C). These results suggested
181 that the activity of TORC1 was necessary for the assembly of Ade4 granules. To further
182 identify the TORC1-related factors responsible for Ade4 granule formation, we observed
183 Ade4-GFP foci in 37 single-gene deletion mutants, each of which lacked one of the 17
184 upstream regulators, the 17 downstream effectors of TORC1 signaling, or 3 genes of
185 interest (Fig. 3S1A-B). Consistent with the inhibitory effects of rapamycin, the assembly
186 of Ade4-GFP foci was liable to be attenuated in mutants of the upstream activators of
187 TORC1 signaling (such as the Pib2 or EGO complex). Most of the downstream effectors
188 of TORC1 signaling appeared to have no or only a negligible effect on Ade4-GFP foci.
189 However, the assembly of the foci and granules of Ade4-mNG was significantly
190 suppressed in *sfp1*Δ and *sit4*Δ cells (Figs. 3D-E and 3S1A-B).
191

192 Sfp1 and Sit4 have both been implicated in cytoplasmic crowding through ribosome
193 biogenesis [27, 29, 30]. Therefore, we examined the importance of ribosome synthesis on Ade4
194 granule formation. Diazaborine has been shown to specifically inhibit the maturation of

195 the 60S ribosomal subunit and reduce the level of the 60S subunit in yeast cells [31]. The
196 treatment of cells with diazaborine strongly suppressed the formation of Ade4-GFP foci
197 and Ade4-mNG granules, suggesting that the active synthesis of the ribosomal 60S
198 subunit is required for the assembly of these condensates (Figs. 3F and 3S1C-D). Taken
199 together, macromolecular crowding of the cytoplasm by TORC1-mediated ribosome
200 synthesis may be the main driving force of phase separation required for the assembly of
201 Ade4 granules.
202

203 ## Intracellular derivatives of purine nucleotides prevent the formation of Ade4
204 condensates

205 Although phase separation driven by macromolecular crowding in the cytoplasm was
206 necessary for the assembly of Ade4 granules, it was only one of the prerequisites. Another
207 layer of regulation is required to enable cells to suppress the assembly of granules in the
208 presence of extracellular purine bases. Purine bases are actively transported into cells by
209 the purine-cytosine permease Fcy2[32] and converted to various metabolites (Fig. 4A).
210 Therefore, we investigated the metabolites responsible for the suppression of Ade4
211 granule formation. Foci were dissolved in wild-type cells with Ade4-GFP foci treated
212 with medium containing adenine or hypoxanthine (Fig. 4B-E, wt). In *aah1*Δ*apt1*Δ cells,
213 in which incorporated adenine was not further metabolized, the addition of hypoxanthine,
214 but not adenine, dissolved Ade4 foci (Fig. 4B-C). These results suggested that
215 intracellular adenine itself did not affect Ade4 granules. In *hpt1*Δ cells in which
216 incorporated hypoxanthine was not further metabolized, the addition of hypoxanthine did
217 not disassemble Ade4 foci, whereas the addition of adenine slightly dissolved the foci
218 (Fig. 4B, D). This result indicated that intracellular hypoxanthine itself did not affect
219 Ade4 granules, and also that intracellular adenine was efficiently converted to
220 hypoxanthine. In *ade12*Δ cells in which IMP was not converted to AMP via
221 adenylosuccinate (S-AMP), the addition of hypoxanthine did not disassemble Ade4 foci,
222 whereas that of adenine moderately dissolved the foci (Fig. 4B, E). The inhibition of
223 Ade12 by alanosine, a specific inhibitor of adenylosuccinate synthetase [33], gave similar
224 results: in alanosine-treated cells, the addition of hypoxanthine partially dissolved Ade4-
225 GFP foci (Fig. 4S1A-C). Based on these results, we concluded that adenine nucleotides,
226 including S-AMP derived from external purine bases, were responsible for inhibiting the
227 assembly of Ade4 condensates in the presence of extracellular purine bases.
228

229 ## Interaction of purine nucleotides with Ade4 is implicated in granule assembly

230 We initially suspected that Ade4 itself was the site of action of the inhibitory adenine

231 nucleotide suppressing its granule assembly because PPATs have been shown to directly
232 bind to purine nucleotides, particularly AMP and GMP [1, 6, 34]. Interactions with these
233 purine nucleotides down-regulate PPATs (see the Introduction). A structural analysis of *B.*
234 *subtilis* PPAT proposed the involvement of K316 and R318 in interactions with adenine
235 nucleotides (Fig. 5A), and the replacement of these residues with glutamine reduced
236 affinity for AMP or GMP[35 34]. Furthermore, D293 has been suggested to interact with
237 purine nucleotides, and the replacement of the residue with valine reduced affinity for
238 purine nucleotides[9]. Structural data showed that these three amino acids formed hydrogen
239 bonds with ADP or GMP (Fig. 5A). These three amino acid residues, and their adjacent
240 amino acid sequences, were well conserved among the PPATs of various species,
241 including budding yeast (Fig. 5B). Therefore, we introduced these corresponding
242 mutations into Ade4 (D310V, K333Q, and R335Q, hereafter Ade4-VQQ) and assessed
243 whether the interaction with purine nucleotides affected the assembly of Ade4 granules.
244 In comparisons with the granules of Ade4-mNG, those of Ade4-VQQ-mNG were
245 detected in a higher percentage of cells (Fig. 5C, D) and had a higher fluorescence
246 intensity (Fig. 5E). These results suggested that the mutant Ade4 was more liable to
247 assemble and condense into granules. In other words, the binding of purine nucleotides
248 to Ade4 may play an inhibitory role in granule assembly.
249

250 ## Ade4 protein condensates into particles under molecular crowding conditions *in*
251 *vitro*

252 Regarding the molecular mechanisms regulating the assembly of Ade4 granules, two
253 mutually exclusive possibilities appeared. The first possibility was that Ade4 itself was
254 sufficient for granule assembly, and the second was that other cellular components
255 (including proteins, lipids, and organelles) were required to assemble Ade4 into granules.
256 To distinguish the two possibilities, we investigated the properties of the pure Ade4
257 protein *in vitro*. A previous study reported that the expression of Ade4 in the active form
258 was negligible in bacteria [36]. Therefore, we purified Ade4-mNG from budding yeast cells
259 (Fig. 6S1A). Using data derived from twenty quantitative proteomic studies, intracellular
260 concentrations of Ade4 were estimated to be approximately 0.5 μM (Fig. 6S2). In
261 subsequent *in vitro* assays, we selected the concentrations of Ade4-mNG that were close
262 to or slightly lower than the estimated concentration. Under physiological ionic
263 conditions (0.15 M NaCl, 4 mM $MgCl_2$, pH 7.5), purified Ade4-mNG homogenously
264 dispersed, showing no aggregates ("0%" in Fig. 6A). We then tested the effects of
265 macromolecular crowding using polyethylene glycol (PEG) as a crowding agent. The
266 addition of PEG8000 induced the formation of sub-micron-sized particles of Ade4-mNG

267 in a concentration-dependent manner; a large amount of particles formed in >10% PEG
268 (Fig. 6A-C). The aggregation of the pure mNG protein was not induced by 10% PEG (Fig.
269 6S1B). We also investigated the effects of PEG sizes and found that Ade4-mNG
270 assembled into particles in the presence of >4 kDa PEG (Fig. 6S1C). Consistent with this
271 size dependency, other crowding agents, 2% lysozyme (MW: 14 kDa) and Ficoll-400
272 (MW: 400 kDa) induced the assembly of Ade4-mNG particles (Fig. 6S1F). These results
273 clearly suggested that Ade4 by itself was capable of assembling into sub-micron particles
274 under macromolecular crowding conditions.
275
276 We then examined the role of phase separation in the self-assembly of Ade4-mNG *in vitro*.
277 In the presence of 1, 6-hexanediol, the mean fluorescence intensity and total mass of
278 Ade4-mNG particles were both significantly reduced (Fig. 6D-F). Similarly, Ade4ΔIDR-
279 mNG self-assembled into particles less effectively than Ade4-mNG (Fig. 6G-I).
280 Therefore, we concluded that Ade4 molecules partially aggregated independently of the
281 IDR moiety, and phase separation was important for the full assembly of Ade4 particles
282 *in vitro*.
283
284 Purine nucleotides attenuate the assembly of Ade4 particles *in vitro*
285 As demonstrated above, purine nucleotides were expected to suppress the aggregation of
286 Ade4 in yeast cells (Figs. 4 and 5). Therefore, we investigated whether purine nucleotides
287 exerted some effects on the *in vitro* assembly of Ade4-mNG particles. In the presence of
288 GMP, AMP, ADP, and ATP, the condensation of Ade4-mNG was significantly reduced
289 (Fig. 7A and Fig. 7S1C). AMP, ADP, and ATP were more effective than GMP, while S-
290 AMP unexpectedly had no significant effect. Adenine and inosine, a degradation product
291 of IMP, did not affect the *in vitro* condensation of Ade4 (Fig. 7S1A-B), which is consistent
292 with *in vivo* results (Fig. 4). More than 250 μM AMP, ADP, or ATP was required to
293 achieve maximal inhibitory effects, whereas the inhibitory effects of GMP plateaued at
294 100 μM (Fig. 7B-D and Fig. 7S1D). Importantly, AMP also inhibited the condensation of
295 Ade4ΔIDR-mNG as well as that of Ade4-mNG (Fig. 7E). These results suggested that
296 purine nucleotides, including AMP, ADP, ATP, and GMP, repressed the condensation of
297 Ade4 molecules by inhibiting IDR-independent aggregation.
298
299 Formation of Ade4 granules is important for efficient *de novo* purine synthesis
300 during cell growth
301 We examined the physiological significance of Ade4 granules. On solid medium in the
302 absence of adenine, the growth of cells expressing Ade4ΔIDR-3HA, which failed to

303 assemble into granules, was markedly slowly than those expressing Ade4-3HA (Fig. 8A).
304 The protein level of Ade4ΔIDR-3HA in cells grown in adenine-free medium was similar
305 to that of Ade4-3HA (Fig. 8B). Supplementation with adenine restored the growth of the
306 *ADE4ΔIDR* mutant to the wild-type rate, indicating that the slow growth of the mutant
307 was due to the limited activity of the enzyme and not to dominant-negative inhibition
308 caused by the mutant protein. We also noted that the phenotype of the *ADE4ΔIDR* mutant
309 depended on the nitrogen source of the medium: the mutant grew more slowly as
310 concentrations of ammonium ions in the medium decreased (Fig. 8A). Therefore, we
311 quantitatively examined cell growth by measuring growth curves in liquid medium. The
312 *ADE4ΔIDR* mutant showed significantly slower growth, particularly in the absence of
313 ammonium ions, whereas the growth rate of the wild-type strain was almost independent
314 of ammonium ion concentrations in the medium (Fig. 8C-D and Fig. 8S1A-B). These
315 results suggested that the formation of Ade4 granules was important for enhancing
316 enzymatic activities in cells to support efficient cell growth, particularly in a low-
317 ammonium environment.
318
319 Biochemical analyses previously revealed that PPAT directly utilized NH_3 as a nitrogen
320 donor in place of glutamine to produce PRA[5]. Glutamine-dependent PRA synthesis (Gln-
321 PRA activity) (Fig. 8S1C) and NH_3-dependent PRA synthesis (NH_3-PRA activity) (Fig.
322 8S1C) have both been implicated in the *de novo* biosynthesis of purine nucleotides *in vivo*
323 [37 38]. Moreover, biochemical assays revealed that NH_3-PRA activity depended on the
324 concentrations of NH_4Cl, a fraction of which was in the form of NH_3, whereas Gln-PRA
325 activity was inhibited by NH_3 [5]. Therefore, Gln-PRA activity and NH_3-PRA activity may
326 be activated in cells under low and high NH_3 (ammonium) conditions, respectively (Fig.
327 8S1C-D). We speculated that the slow ammonium concentration-dependent growth of the
328 granule-hypoplasia *ADE4ΔIDR* mutant was due to the inefficient enhancement of the
329 Gln-PRA activity of Ade4.
330
331 MD calculations predict the possible leakage of glutamine-derived NH_3 from
332 PPAT molecules
333 In the process of PRA synthesis from glutamine, NH_3 is drawn from glutamine at the first
334 glutamine amidotransferase (GATase) site and then needs to be efficiently transferred to
335 PRPP loaded on the second phosphoribosyltransferase (PRTase) site to prevent the release
336 of intermediate NH_3 into bulk solution. A structural analysis of *E. coli* PPAT suggested
337 that the binding of PRPP activated PPAT and resulted in the formation of a hydrophobic
338 channel connecting the GATase and PRTase sites [39]. Therefore, the channel was expected

339 to permit the efficient intramolecular transfer of the intermediate NH_3 between the two
340 catalytic sites (Figs. 9F, H and 9S1A). However, we hypothesized that the extreme
341 condensation of granules enabled the intermolecular transfer of the intermediate NH_3
342 between Ade4 molecules and, hence, promoted Gln-PRA activity. Therefore, we
343 investigated whether glutamine-derived NH_3 escaped from the initial site through paths
344 other than the intramolecular channel by examining the behavior of NH_3 on the PPAT
345 molecule using a molecular dynamics (MD) simulation. The calculation of MD was based
346 on the crystal structure of *E. coli* PPAT in the active form (PDB: 1ECC) [39].
347
348 We performed MD simulations for the holo condition of PPAT that contained glutamic
349 acid, NH_3, PRPP, and Mg^{2+}. During ten individual trials, NH_3 was not released from PPAT
350 and remained in the initial or adjacent positions (Fig. 9A). NH_3 did not reach the catalytic
351 site. We then performed MD simulations for the semi-holo condition that contained only
352 glutamic acid and NH_3. NH_3 was released through the hydrophobic channel once in the
353 ten trials. NH_3 was released through a transient channel that was directed to Arg333,
354 which was conserved in Ade4, hereinafter referred to as the front channel, four times in
355 ten trials (Fig. 9B, D). Prior to the release of NH_3, a hydrophobic side chain of Phe260
356 was flipped from the initial structure. Furthermore, Arg333 functioned as a gate for NH_3
357 and water by forming hydrogen bonds with the backbone oxygen of Tyr259, Phe260,
358 His26, and the phosphate group of PRPP (Fig. 9D, E). In the semi-holo condition, the
359 lack of PRPP opened the Arg gate. To confirm the existence of the Arg gate, additional
360 MD simulations were performed on the Arg333Ala mutant under the holo condition. As
361 expected, the flipping of the Phe260 side chain and NH_3 release were both observed six
362 times in ten trials even though PRPP was in the catalytic site (Fig. 9C).
363
364 These results suggested that after the production of NH_3 from glutamine, the attack of
365 external NH_3 released PRA, which opened the Arg gate, making the front channel, and
366 internal NH_3 then escaped from the channel (Fig. 9G and 9S1C).
367

368 **Discussion**

369 We herein demonstrated that the budding yeast PPAT Ade4 formed intracellular fine
370 granules in purine-depleted media. These granules were highly dynamic and possessed
371 liquid-like properties, and phase separation was involved in granule assembly. We also
372 showed that phase separation was driven by the molecular crowding of the cytoplasm
373 induced by active TORC1 and its downstream ribosome biogenesis. Purified Ade4 self-
374 assembled into sub-micron-sized particles, and sub-millimolar purine nucleotides
375 inhibited the formation of particles, as indicated by the genetic analysis. Cells unable to
376 form Ade4 granules showed slower growth, suggesting the importance of the granules
377 for the promotion of *de novo* purine synthesis. The MD simulation implied the
378 condensation-dependent activation of PPAT by enabling the intermolecular channeling
379 of the intermediate NH_3. These results indicate that the formation of Ade4 granules is a
380 biologically relevant mechanism that regulates purine synthesis in response to both
381 TORC1 activity and purine nucleotide levels.
382
383 We visualized intracellular fine granules of the budding yeast Ade4 using the bright,
384 monomeric fluorescent protein mNG. These structures were overlooked in previous
385 studies in which Ade4 was tagged with non-monomeric GFP[20, 22]. The large foci of
386 Ade4 reported in previous studies and granules appeared to share basic properties;
387 however, since the pure Ade4 protein assembles into granule-sized particles, the latter is
388 likely to be the actual structure of Ade4. A close examination of granules revealed their
389 inherently dynamic nature in that they quickly assembled or disassembled in response to
390 environmental purine bases.
391
392 A previous study demonstrated that Ade4 played an indirect, but pivotal role in
393 regulating the expression of AMP biosynthesis genes in response to extracellular purine
394 bases [36]. The present results suggest that Ade4 is also crucial for the more rapid, short-
395 term regulation of purine biosynthesis, in addition to its long-term regulation at the
396 transcriptional level.
397

398 Assembly mechanism of Ade4 granules

399 We found that phase separation dependent on both TORC1 activity and the C-terminal
400 IDR of Ade4 was essential for the assembly of Ade4 granules. In addition, we identified
401 Sfp1 and Sit4 as genes downstream of TORC1 that are critically involved in granule
402 assembly. Since both genes are important for ribosome synthesis, the requirement of
403 ribosome synthesis for granule assembly was tested and confirmed. These results are

404 consistent with the theory that TORC1 regulates the macromolecular crowding of the
405 cytoplasm through ribosome synthesis and degradation, which, in turn, controls
406 biomolecular condensation by phase separation [27]. This study is the first experimental
407 demonstration of a metabolic enzyme assembling into condensates by the TORC1-
408 regulated phase transition of the cytoplasm in yeast cells (Figure 7F, left panel). Since
409 TORC1 and PPAT IDRs are both conserved in many species, the condensation of PPAT
410 by TORC1 may be a common feature in eukaryotic cells.
411
412 Purified Ade4 was capable of self-assembling into fine particles under molecular
413 crowding conditions. Therefore, we speculated that Ade4 by itself also assembled into
414 granules in cells; however, unidentified auxiliary factors may participate in their
415 assembly. *In vitro* assays also revealed that the condensation of Ade4 comprised IDR-
416 independent aggregation and IDR-dependent phase separation. The former may be a
417 prerequisite for the latter (Fig. 7F, right panel). IDR-independent aggregates were small
418 and appeared to be unstable in living cells and, hence, were undetectable (Fig. 2D).
419 Phase separation may be required for the stable condensation of aggregates into
420 granules. There was a threshold size and concentration of PEG required to induce the
421 formation of Ade4 particles *in vitro*, which suggested that the assembly of Ade4
422 granules is only allowed within a narrow range of ribosome concentrations *in vivo*.
423
424 The genetic analysis indicated an inhibitory role for purine nucleotides in the assembly
425 of Ade4 granules, and purine nucleotides suppressed the IDR-independent aggregation
426 of Ade4 *in vitro*. Therefore, we speculated that the intracellular purine nucleotide
427 concentration, which fluctuates in response to extracellular purine bases, controlled the
428 assembly of Ade4 granules as another regulatory layer of PPAT activity (Fig. 7F, right
429 panel). Human PPAT has been shown to form an inactive tetramer in complex with
430 AMP, but an active dimer in the apo form. [7, 40]. Moreover, human PPAT bearing a
431 mutation that corresponds to K333Q, one of the VQQ mutations, predominantly formed
432 active dimers, even in the presence of AMP[7]. Therefore, interactions with purine
433 nucleotides are closely associated with the transition between the dimer and tetramer in
434 eukaryotic PPAT. The present results further suggest that dimers (depicted by hexagons
435 on the right in Fig. 7F), but not tetramers (depicted by circles), are prone to aggregate
436 under molecular crowding conditions. This model indicates that the affinity of each
437 purine nucleotide for Ade4 affects the strength of inhibition. Satyanarayana and Kaplan
438 reported that AMP, ADP, and ATP inhibited the enzymatic activity of partially purified
439 Ade4 more strongly than GMP [41], which is consistent with the present results.

440

441 Biological significance of Ade4 granules

442 The condensation of Ade4 into granules is of physiological significance because cells
443 devoid of granules show slower growth as environmental NH_3 levels decrease. This
444 phenotype is suppressed in the presence of purine bases, in which purine synthesis
445 through the salvage pathway is available. This suggests that condensation activates the
446 rate-limiting enzyme Ade4 and, thus, is important for the activation of *de novo* purine
447 synthesis. Under low ammonium conditions, it is more important to use glutamine as a
448 substrate. We hypothesized that condensation promotes the Gln-PRA activity of Ade4.
449 The MD simulation revealed a previously unidentified path through which glutamine-
450 derived intermediate NH_3 leaked out of the PPAT molecule (Figs. 9G and 9S1C). By its
451 nature, the NH_3 molecule rapidly diffuses throughout the cytoplasm. However, in Ade4
452 granules, in which the local concentration of the enzyme is very high, another enzyme
453 was more likely to trap NH_3 and process it by the PRTase domain (Figs. 9H and 9S1D).
454 In other words, since the transfer efficiency of the intermediate NH_3 is not necessarily
455 perfect, the condensation of Ade4 with two catalytic domains is equivalent to the co-
456 clustering of two enzymes having GATase and PRTase, respectively, in the microspace.
457 This type of activation by intermolecular NH_3 channeling corresponds to the clustering-
458 mediated metabolic channeling (of intermediates) demonstrated theoretically and
459 experimentally by Castellana et al [42].

460

461 The activity of PPAT is known to be regulated in a feedback manner by millimolar
462 levels of AMP and GMP *in vivo* [43]. However, since intracellular purine mononucleotide
463 concentrations are generally in the micromolar range of tens to hundreds, this regulation
464 does not appear to be physiologically relevant. The present study elucidated a
465 mechanism that regulates intracellular PPAT activity in a more acute, sensitive, and
466 physiologically valid manner.

467

468 TORC1 is activated by sensing nutrients, such as amino acids, glucose, and ATP [44].
469 Therefore, the requirement of TORC1 activity for PPAT condensation ensures that the
470 *de novo* synthesis of purines is only up-regulated under conditions that are favorable for
471 cell growth. A previous study also reported that mammalian TORC1 transcriptionally
472 up-regulated enzymes involved in the mitochondrial tetrahydrofolate cycle, thereby
473 increasing *de novo* purine synthesis [45]. Correlating the metabolic flux of purine
474 synthesis with the nutritional status via TORC1 activity appears to be a conserved and
475 elaborate strategy for cell proliferation.

Recent studies showed that many metabolic enzymes formed intracellular condensates by phase separation, allowing cell metabolism to adapt to changing growth conditions. [11]. These condensates were mostly a temporary store of inactive enzymes to survive adverse environmental conditions and, in a few cases, an activated form of enzymes. As already described in the Introduction, human CTPS polymerizes into filaments with an active conformation[18]. Mammalian acetyl-CoA carboxylate 1 (ACC1) has also been shown to form filamentous structures *in vivo* and *in vitro* for decades. A recent study revealed that filament formation in the presence of citrate locked human ACC1 into an active conformation[46]. The present results provide another example where the condensation of a metabolic enzyme leads to its activation. Ade4 condensation is unique in that it forms highly dynamic structures and activates its enzymatic activity through the cluster-mediated channeling of intermediates. Although Ade4 does not appear to polymerize into filaments, future research is awaited to elucidate the molecular organization within granules. A more detailed understanding of the architecture of PPAT condensates will provide insights into the mechanism of condensation. Based on that information, PPAT condensation has potential as a therapeutic target for diseases associated with abnormal purine metabolism, such as cancer and gout.

495 **Materials and Methods**

496 Yeast strains and plasmids

497 The yeast strains, plasmids, and primers used in the present study are listed in
498 Supplementary Tables S1, S2, and S3 respectively. These strains were constructed by a
499 PCR-based method [47] and genetic crosses. The yeast knockout strain collection was
500 originally purchased from GE Healthcare (cat. # YSC1053).
501
502 Regarding the construction of plasmids used for the C-terminal tagging of monomeric
503 GFP or mKate2, DNA fragments encoding the corresponding fluorescent proteins were
504 artificially synthesized (Eurofin Genomics, Ebersberg, Germany). These fragments
505 were replaced with GFP of pYM25[47] using *Sal*I/*Bgl*II sites to yield MTP3114 and
506 MTP3131, respectively. The plasmid used for the C-terminal tagging of mNG-Strep tag
507 II (MTP3139) was constructed in the same manner: a DNA fragment encoding single
508 mNG fused with the Strep II tag (WSHPQFEK) by a spacer sequence (ELYKGSA) was
509 synthesized and then replaced with the GFP of pYM25.
510

511 Media and cell culture

512 Synthetic medium optimized for the growth of the BY strain was prepared as described
513 by Hanscho et al. [48]. Growth assays in solid and liquid media used optimized synthetic
514 media lacking glutamate, phenylalanine, serine, and threonine. Yeast nitrogen base
515 without amino acids, but with ammonium sulfate (cat. # Q30009) was purchased from
516 Invitrogen. Yeast nitrogen base without amino acids and ammonium sulfate (cat. #
517 CYN0501) was purchased from FORMEDIUM. Rich medium was standard YPD
518 medium composed of 1% (w/v) yeast extract (BD, cat. # 212750), 2% (w/v) bacto-
519 peptone (BD, cat. # 211677), and 2% (w/v) D-glucose. Glucose (cat. # 049-31165),
520 adenine sulfate (cat. # 018-10613), hypoxanthine (cat. # 086-03403), 1, 6-hexanediol
521 (cat. # 087-00432), and digitonin (cat. # 043-2137) were purchased from FUJIFILM
522 Wako. Cells were grown to the mid-log phase at 30°C before imaging unless otherwise
523 noted. To replace medium containing adenine with medium lacking adenine, cells were
524 collected in a microtube by brief centrifugation and suspended in medium lacking
525 adenine. This washing procedure was repeated at least twice. Rapamycin was purchased
526 from LC Laboratories (cat. # R-5000).
527

528 Microscopy

529 Cells expressing a GFP-fusion protein were concentrated by centrifugation and
530 sandwiched between a slide and coverslip (No. 1.5 thickness, Matsunami, Osaka,

531 Japan). Immobilized cells were imaged using an inverted fluorescent microscope
532 (Eclipse Ti2-E, Nikon, Tokyo, Japan) equipped with a CFI Plan Apoλ 100× Oil
533 DIC/NA1.45 objective lens and CMOS image sensor (DS-Qi2, Nikon). The fluorescent
534 signal was collected from stacks of 11 *z*-sections spaced by 0.5 μm, and the maximum
535 projections of the optical sections were shown unless otherwise noted. A CFI Plan Apoλ
536 60× Oil Ph3 DM/NA1.40 or CFI Plan Apoλ 100× Oil Ph3 DM/NA1.45 objective lens
537 was used for phase contrast imaging. Images of cells were acquired from several fields
538 of view for each experimental condition. All digital images were processed with the Fiji
539 image platform[49].
540

541 Quantitative analysis of intracellular fluorescent condensation

542 Intracellular fluorescent condensation (*i.e.*, Ade4-GFP foci or Ade4-mNG granules) was
543 automatically detected and analyzed by running Fiji macros
544 (https://github.com/masaktakaine/FP-foci-quantification and
545 https://github.com/masaktakaine/FP-granules-quantification). Briefly, these macro
546 extract cell outlines from phase-contrast images and detect fluorescent condensation
547 inside the cell boundary using the *FindMaxima* function of Fiji software.
548
549 To monitor temporal changes in the number of intracellular Ade4-mNG granules by
550 time-lapse imaging, the number of maxima of green fluorescence intensity in the field
551 was counted in each time frame and divided by the total cell number by running a Fiji
552 macro (https://github.com/masaktakaine/Counting-FP-granules-in-time-lapse).
553 In cases in which phase-contrast images were unavailable, we manually examined
554 condensation.
555

556 Spot growth assay

557 Cells were grown to the mid-log phase at 30°C in synthetic medium, and cell density
558 (cells/ml) was measured by an automated cell counter (TC20, Bio-Rad). The culture
559 was diluted by medium lacking nitrogen and carbon sources to a density of 1×10^6
560 cells/ml, serially diluted 5-fold, and spotted on plates. Plates were incubated for 2-3
561 days at 30°C and then imaged by an image scanner (GT-X830, EPSON).
562

563 Measurement of growth curves in a liquid culture

564 Cell growth in liquid media was monitored in a 96-well flat-bottomed plate using a
565 microplate reader (iMark, Bio-Rad). Cells were grown to the mid-log phase and then

566 diluted to OD_{600} = 0.1. Each well was filled with 300 μl of the cell dilution and OD_{595}
567 was measured at 30°C every 10 min.
568
569 Immunoblot analysis
570 A denatured whole-cell extract was prepared according to the method reported by von der
571 Haar (2007) [50]. Briefly, mid-log cells were harvested from 2–3 ml of the culture by
572 centrifugation. The cell pellet was resuspended in a small volume (<100 μl) of lysis buffer
573 (0.1 M NaOH, 50 mM EDTA, 2% (w/v) SDS, and 2% (v/v) β-mercaptoethanol) and then
574 incubated at 90°C for 10 min. The sample was neutralized by the addition of a one-tenth
575 volume of 1 M acetic acid, incubated at 90°C for 10 min, and mixed with a one-third
576 volume of 4×Laemmli protein sample buffer (cat. # 1610747, Bio-Rad). Following
577 centrifugation at 20,000×*g* at 4°C for 10 min, the upper 90% of the supernatant was
578 collected as the clarified whole-cell extract and stored at -30°C until used. Proteins were
579 resolved by SDS-PAGE using a pre-cast gel containing 10% (w/v) acrylamide
580 (SuperSep™ Ace, cat. # 195-14951, FUJIFILM Wako) and then transferred onto a PVDF
581 membrane (Immobilon-P, Millipore) using a protein transfer system (Trans-Blot Turbo
582 Transfer System, Bio-Rad). HA-tagged Ade4 proteins were detected using an anti-HA
583 antibody (mouse monoclonal (12CA5), cat. # GTX16918, Funakoshi) at a 1:1000 dilution.
584 GFP-tagged proteins were detected using an anti-GFP antibody (mouse monoclonal
585 (1E10H7), cat. #66002-1-Ig, ProteinTech) at a 1:1000 dilution. GAPDH was detected
586 using an anti-GAPDH antibody (mouse monoclonal (1E6D9), cat. # 60004-1-Ig,
587 ProteinTech) at a 1:1000 dilution. PGK1 was detected using an anti-PGK1 antibody
588 (mouse monoclonal (22C5D8), cat. # ab113687, Abcam) at a 1:1000 dilution. An HRP-
589 conjugated secondary antibody (from sheep, cat. #NA931V, GE Healthcare) was probed
590 at a 1:10000 dilution. Immunoreactive bands were luminescent in a chemiluminescent
591 substrate (Western BLoT Quant HRP substrate, cat. # T7102A, TaKaRa) and imaged
592 using an image analyzer (LAS4000, GE Healthcare).
593
594 Protein purification from yeast cells
595 Ade4-mNG, Ade4ΔIDR-mNG, and mNG were C-terminally tagged with a single Strep-
596 tag II, expressed in budding yeast cells, and purified as follows. Yeast cells expressing
597 the tagged protein were grown in liquid YPD medium supplemented with 0.02 mg/ml
598 adenine sulfate at 30°C for at least 20 h. The pre-culture was diluted by 100–1000-fold in
599 100 ml of fresh YPD plus adenine medium, and cells were further grown at 30°C to 4×10^7
600 cells/ml. Cells were harvested by centrifugation at 2,000×*g* and washed twice with 1 ml
601 of extraction buffer (EB) (0.15 M NaCl, 1 mM EDTA, 1 mM dithiothreitol, and 40 mM

602 Tris-HCl, pH 7.5) supplemented with 1 mM PMSF and cOmplete protease inhibitor
603 cocktail (EDTA-free) (Roche, cat. # 11836170001). One gram of glass beads with a
604 diameter of 0.5 mm (YASUI KIKAI, cat. # YGBLA05) was mixed with the cell
605 suspension, and cells were disrupted by vigorous shaking using a beads beater (YASUI
606 KIKAI, MB901). The crude cell extract was collected by brief centrifugation, and glass
607 beads were washed with a small volume of EB (<0.5 ml). The crude extract and washings
608 were combined and clarified by centrifugation twice at 20,000×*g* at 4°C for 10 min. To
609 block endogenous biotin, the cleared lysate was supplemented with 0.2 mg/ml neutralized
610 avidin (FUJIFILM Wako, cat. # 015-24231), incubated on ice for 30 min, and clarified
611 by centrifugation at 20,000×*g* at 4°C for 10 min. The supernatant was loaded onto a
612 handmade open column packed with 0.5 ml of Strep-Tactin Sepharose (IBA GmbH, cat.
613 # 2-1201-002). After washing with 10 column volumes of EB, bound proteins were eluted
614 with 6 column volumes of EB plus 2.5 mM D-desthiobiotin (IBA GmbH, cat. # 2-1000-
615 025). The protein amounts and compositions of elution fractions were analyzed by SDS-
616 10% PAGE and stained with FastGene Q-stain (Nippon Genetics, cat. # NE-FG-QS1).
617 Peak fractions were pooled and concentrated using an Amicon Ultra-0.5 centrifugal filter
618 device with a molecular weight cut-off of 30 or 10 kDa (Merck, cat. # UFC503024 or
619 UFC501008). D-desthiobiotin in the peak fraction was diluted more than 100-fold by a
620 repeating dilution with EB and the centrifugal concentration. The concentration of the
621 purified protein was assessed by densitometry using bovine serum albumin (TaKaRa, cat.
622 # T9310A) as a standard following SDS-PAGE and staining with the Q-stain. Purified
623 Ade4-mNG and Ade4ΔIDR-mNG were supplemented with 5 and 10 mM DTT and stored
624 on ice.
625
626 *In vitro* condensation assay
627 The purified protein was diluted to the indicated concentration in assay buffer (EB plus
628 5 mM $MgCl_2$) and supplemented with 0–15% (w/v) PEG 8000 (FUJIFILM Wako, cat. #
629 596-09755). In the experiments shown in Fig. 6S1C, samples were spiked with 10%
630 (w/v) PEG of the indicated molecular size. The mixture was immediately loaded into an
631 assay chamber composed of a glass slide and coverslip attached by double-sided tape.
632 Fluorescent condensation was imaged using the Nikon inverted fluorescent microscope
633 (see above). Images of fluorescent condensation were analyzed by running a Fiji macro
634 (https://github.com/masaktakaine/In-vitro-condensates-quantification). Briefly, the
635 macro automatically detects fluorescent condensation and quantifies its area and
636 fluorescence intensity.
637

MD simulation

The crystal structure of *E. coli* PPAT (PDB ID: 1ECC) was obtained from the Protein Data Bank and used for all MD simulations [39]. All water molecules and ions were removed before simulations. To build the parameters of ligands (NH_3, PRPP, and glutamic acid), their restrained electrostatic potential charges were calculated based on gas-phase HF/6-31(d) quantum mechanics calculations using Gaussian 16. A set of parameters were generated with a general AMBER force field using the antechamber from AMBER tools [51].

The Amber 14SB force field was employed for all MD simulations [52]. Missing hydrogen atoms were added by LEaP from AMBER tools. Proteins were solvated with the TIP3P water box [53]. The system was neutralized by replacing water with Na^+ or Cl^- ions. The particle-mesh Ewald (PME) method was employed for the Coulomb interaction [54]. Amber-formatted input files were converted for GROMACS using acpype [55]. All MD simulations were performed using GROMACS 2019.6 [56]. Before the production run, three-step equilibrations were performed for each system. Energy minimization was performed until 10,000 steps. This was followed by 100-ps *NVT* equilibration with the V-rescale thermostat [57] at 300 K under 1 atm. A 100-ps *NPT* equilibration was then conducted with Berendsen coupling [58] at 300 K under 1 atm. A run was performed under the *NPT* condition. The time step of each simulation was 2 fs with the SHAKE [59] and SETTLE [60] algorithms, and the snapshot was recorded every 100 ps during the production run. To examine the results of MD simulations, a Python library MDanalysis was used [61].

Data analysis

Numerical data were plotted using R studio software (R ver. 4.2.0) [62]. Means, SDs, and *p* values were calculated using Excel software (Microsoft, WA, US) and the R studio. The significance of differences between two sets of data was tested using the unpaired two-tailed Welch's *t*-test unless otherwise noted and was indicated by an asterisk or *p* value. The horizontal bar in the dot plot indicates the average of each population. All measurements were repeated at least twice to confirm reproducibility.

Acknowledgments

The authors thank the IMCR-JURSC in Gunma University for sharing research equipment. This work was supported by research grants from the Gout and Uric Acid Foundation of Japan and by JSPS KAKENHI Grant Number JP22K06216 to M.T. This study used the computational resources of Cygnus provided by the Multidisciplinary Cooperative Research Program at the Center for Computational Sciences (Project Code: MOLBIO), University of Tsukuba.

Author Contributions

MT conceived and supervised the study, MT and RM designed the experiments, MT performed the experiments, RM performed MD simulations, MT and RM analyzed the data, MT wrote the manuscript draft with input from RM, and MT and RM revised the manuscript.

Declaration of Interests

The authors declare no competing interests.

686 **References**

687 1. Yamaoka, T. *et al.* Amidophosphoribosyltransferase Limits the Rate of Cell Growth-linked de
688 Novo Purine Biosynthesis in the Presence of Constant Capacity of Salvage Purine Biosynthesis.
689 *Journal of Biological Chemistry* **272**, 17719-17725 (1997).
690 2. Daignan-Fornier, B. & Pinson, B. Yeast to Study Human Purine Metabolism Diseases. *Cells* **8**
691 (2019).
692 3. Pareek, V., Pedley, A.M. & Benkovic, S.J. Human de novo purine biosynthesis. *Crit Rev Biochem*
693 *Mol Biol*, 1-16 (2020).
694 4. Smith, J.L. *et al.* Structure of the allosteric regulatory enzyme of purine biosynthesis. *Science* **264**,
695 1427-1433 (1994).
696 5. Messenger, L.J. & Zalkin, H. Glutamine phosphoribosylpyrophosphate amidotransferase from
697 Escherichia coli. Purification and properties. *J Biol Chem* **254**, 3382-3392 (1979).
698 6. Meyer, E. & Switzer, R.L. Regulation of Bacillus subtilis glutamine phosphoribosylpyrophosphate
699 amidotransferase activity by end products. *J Biol Chem* **254**, 5397-5402 (1979).
700 7. Yamaoka, T. *et al.* Feedback inhibition of amidophosphoribosyltransferase regulates the rate of
701 cell growth via purine nucleotide, DNA, and protein syntheses. *J Biol Chem* **276**, 21285-21291
702 (2001).
703 8. Mantsala, P. & Zalkin, H. Glutamine nucleotide sequence of Saccharomyces cerevisiae ADE4
704 encoding phosphoribosylpyrophosphate amidotransferase. *J Biol Chem* **259**, 8478-8484 (1984).
705 9. Jimenez, A., Santos, M.A., Pompejus, M. & Revuelta, J.L. Metabolic engineering of the purine
706 pathway for riboflavin production in Ashbya gossypii. *Appl Environ Microbiol* **71**, 5743-5751
707 (2005).
708 10. Park, J.O. *et al.* Metabolite concentrations, fluxes and free energies imply efficient enzyme usage.
709 *Nat Chem Biol* **12**, 482-489 (2016).
710 11. Prouteau, M. & Loewith, R. Regulation of Cellular Metabolism through Phase Separation of
711 Enzymes. *Biomolecules* **8** (2018).
712 12. Cereghetti, G. *et al.* Reversible amyloids of pyruvate kinase couple cell metabolism and stress
713 granule disassembly. *Nat Cell Biol* **23**, 1085-1094 (2021).
714 13. Saad, S. *et al.* Reversible protein aggregation is a protective mechanism to ensure cell cycle restart
715 after stress. *Nature Cell Biology* **19**, 1202 (2017).
716 14. Noree, C., Monfort, E., Shiau, A.K. & Wilhelm, J.E. Common regulatory control of CTP synthase
717 enzyme activity and filament formation. *Molecular Biology of the Cell* **25**, 2282-2290 (2014).
718 15. Azzam, G. & Liu, J.L. Only one isoform of Drosophila melanogaster CTP synthase forms the
719 cytoophidium. *PLoS Genet* **9**, e1003256 (2013).
720 16. Chen, K. *et al.* Glutamine analogs promote cytoophidium assembly in human and Drosophila cells.
721 *J Genet Genomics* **38**, 391-402 (2011).

722 17. Ingerson-Mahar, M., Briegel, A., Werner, J.N., Jensen, G.J. & Gitai, Z. The metabolic enzyme
723 CTP synthase forms cytoskeletal filaments. *Nat Cell Biol* **12**, 739-746 (2010).
724 18. Lynch, E.M. *et al.* Human CTP synthase filament structure reveals the active enzyme conformation.
725 *Nat Struct Mol Biol* **24**, 507-514 (2017).
726 19. Habrian, C. *et al.* Inhibition of Escherichia coli CTP Synthetase by NADH and Other
727 Nicotinamides and Their Mutual Interactions with CTP and GTP. *Biochemistry* **55**, 5554-5565
728 (2016).
729 20. Narayanaswamy, R. *et al.* Widespread reorganization of metabolic enzymes into reversible
730 assemblies upon nutrient starvation. *Proc Natl Acad Sci U S A* **106**, 10147-10152 (2009).
731 21. An, S., Kumar, R., Sheets, E.D. & Benkovic, S.J. Reversible compartmentalization of de novo
732 purine biosynthetic complexes in living cells. *Science* **320**, 103-106 (2008).
733 22. Noree, C. *et al.* A quantitative screen for metabolic enzyme structures reveals patterns of assembly
734 across the yeast metabolic network. *Mol Biol Cell* **30**, 2721-2736 (2019).
735 23. Zacharias, D.A., Violin, J.D., Newton, A.C. & Tsien, R.Y. Partitioning of lipid-modified
736 monomeric GFPs into membrane microdomains of live cells. *Science* **296**, 913-916 (2002).
737 24. Kroschwald, S., Maharana, S. & Simon, A. Hexanediol: a chemical probe to investigate the
738 material properties of membrane-less compartments. *Matters* (2017).
739 25. Uversky, V.N. Intrinsically disordered proteins in overcrowded milieu: Membrane-less organelles,
740 phase separation, and intrinsic disorder. *Curr Opin Struct Biol* **44**, 18-30 (2017).
741 26. Jones, D.T. & Cozzetto, D. DISOPRED3: precise disordered region predictions with annotated
742 protein-binding activity. *Bioinformatics* **31**, 857-863 (2015).
743 27. Delarue, M. *et al.* mTORC1 Controls Phase Separation and the Biophysical Properties of the
744 Cytoplasm by Tuning Crowding. *Cell* **174**, 338-349.e320 (2018).
745 28. Heitman, J., Movva, N.R. & Hall, M.N. Targets for cell cycle arrest by the immunosuppressant
746 rapamycin in yeast. *Science* **253**, 905-909 (1991).
747 29. Lempiainen, H. *et al.* Sfp1 interaction with TORC1 and Mrs6 reveals feedback regulation on TOR
748 signaling. *Mol Cell* **33**, 704-716 (2009).
749 30. Fingerman, I., Nagaraj, V., Norris, D. & Vershon, A.K. Sfp1 plays a key role in yeast ribosome
750 biogenesis. *Eukaryot Cell* **2**, 1061-1068 (2003).
751 31. Pertschy, B. *et al.* Diazaborine Treatment of Yeast Cells Inhibits Maturation of the 60S Ribosomal
752 Subunit. *Molecular and Cellular Biology* **24**, 6476-6487 (2004).
753 32. Ferreira, T., Brethes, D., Pinson, B., Napias, C. & Chevallier, J. Functional analysis of mutated
754 purine-cytosine permease from Saccharomyces cerevisiae. A possible role of the hydrophilic
755 segment 371-377 in the active carrier conformation. *J Biol Chem* **272**, 9697-9702 (1997).
756 33. Jayaram, H.N. *et al.* Metabolites of alanosine, an antitumor antibiotic. *Biochem Pharmacol* **28**,
757 3551-3566 (1979).

758 34. Zhou, G., Smith, J.L. & Zalkin, H. Binding of purine nucleotides to two regulatory sites results in
759 synergistic feedback inhibition of glutamine 5-phosphoribosylpyrophosphate amidotransferase. *J*
760 *Biol Chem* **269**, 6784-6789 (1994).
761 35. Chen, S. *et al.* Mechanism of the synergistic end-product regulation of Bacillus subtilis glutamine
762 phosphoribosylpyrophosphate amidotransferase by nucleotides. *Biochemistry* **36**, 10718-10726
763 (1997).
764 36. Rebora, K., Desmoucelles, C., Borne, F., Pinson, B. & Daignan-Fornier, B. Yeast AMP pathway
765 genes respond to adenine through regulated synthesis of a metabolic intermediate. *Mol Cell Biol*
766 **21**, 7901-7912 (2001).
767 37. Mantsala, P. & Zalkin, H. Glutamine amidotransferase function. Replacement of the active-site
768 cysteine in glutamine phosphoribosylpyrophosphate amidotransferase by site-directed
769 mutagenesis. *J Biol Chem* **259**, 14230-14236 (1984).
770 38. Mei, B. & Zalkin, H. A cysteine-histidine-aspartate catalytic triad is involved in glutamine amide
771 transfer function in purF-type glutamine amidotransferases. *Journal of Biological Chemistry* **264**,
772 16613-16619 (1989).
773 39. Krahn, J.M. *et al.* Coupled formation of an amidotransferase interdomain ammonia channel and a
774 phosphoribosyltransferase active site. *Biochemistry* **36**, 11061-11068 (1997).
775 40. Holmes, E.W., McDonald, J.A., McCord, J.M., Wyngaarden, J.B. & Kelley, W.N. Human
776 glutamine phosphoribosylpyrophosphate amidotransferase. Kinetic and regulatory properties. *J*
777 *Biol Chem* **248**, 144-150 (1973).
778 41. Satyanarayana, T. & Kaplan, J.G. Regulation of the purine pathway in bakers yeast: activity and
779 feedback inhibition of phosphoribosyl-pyrophosphate amidotransferase. *Arch Biochem Biophys*
780 **142**, 40-47 (1971).
781 42. Castellana, M. *et al.* Enzyme clustering accelerates processing of intermediates through metabolic
782 channeling. *Nature Biotechnology* **32**, 1011-+ (2014).
783 43. Rodwell, V.W., Bender, D., Botham, K.M., Kennelly, P.J. & Weil, P.A. *Harpers Illustrated*
784 *Biochemistry 30th Edition*. (McGraw Hill LLC, 2015).
785 44. Takahara, T., Amemiya, Y., Sugiyama, R., Maki, M. & Shibata, H. Amino acid-dependent control
786 of mTORC1 signaling: a variety of regulatory modes. *Journal of Biomedical Science* **27**, 87 (2020).
787 45. Ben-Sahra, I., Hoxhaj, G., Ricoult, S.J.H., Asara, J.M. & Manning, B.D. mTORC1 induces purine
788 synthesis through control of the mitochondrial tetrahydrofolate cycle. *Science* **351**, 728-733 (2016).
789 46. Hunkeler, M. *et al.* Structural basis for regulation of human acetyl-CoA carboxylase. *Nature* **558**,
790 470-474 (2018).
791 47. Janke, C. *et al.* A versatile toolbox for PCR-based tagging of yeast genes: new fluorescent proteins,
792 more markers and promoter substitution cassettes. *Yeast* **21**, 947-962 (2004).
793 48. Hanscho, M. *et al.* Nutritional requirements of the BY series of Saccharomyces cerevisiae strains

for optimum growth. *FEMS Yeast Res* **12**, 796-808 (2012).

49. Schindelin, J. *et al.* Fiji: an open-source platform for biological-image analysis. *Nat Methods* **9**, 676-682 (2012).

50. von der Haar, T. Optimized protein extraction for quantitative proteomics of yeasts. *PLoS One* **2**, e1078 (2007).

51. D.A. Case, H.M.A., K. Belfon, I.Y. Ben-Shalom, J.T. Berryman, S.R. Brozell, D.S. Cerutti, T.E. Cheatham, III, G.A. Cisneros, V.W.D. Cruzeiro, T.A. Darden, R.E. Duke, G. Giambasu, M.K. Gilson, H. Gohlke, A.W. Goetz, R. Harris, S. Izadi, S.A. Izmailov, K. Kasavajhala, M.C. Kaymak, E. King, A. Kovalenko, T. Kurtzman, T.S. Lee, S. LeGrand, P. Li, C. Lin, J. Liu, T. Luchko, R. Luo, M. Machado, V. Man, M. Manathunga, K.M. Merz, Y. Miao, O. Mikhailovskii, G. Monard, H. Nguyen, K.A. O'Hearn, A. Onufriev, F. Pan, S. Pantano, R. Qi, A. Rahnamoun, D.R. Roe, A. Roitberg, C. Sagui, S. Schott-Verdugo, A. Shajan, J. Shen, C.L. Simmerling, N.R. Skrynnikov, J. Smith, J. Swails, R.C. Walker, J Wang, J. Wang, H. Wei, R.M. Wolf, X. Wu, Y. Xiong, Y. Xue, D.M. York, S. Zhao, and P.A. Kollman (University of California, San Francisco.; 2022).

52. Maier, J.A. *et al.* ff14SB: Improving the Accuracy of Protein Side Chain and Backbone Parameters from ff99SB. *J Chem Theory Comput* **11**, 3696-3713 (2015).

53. Kiss, P.T. & Baranyai, A. Sources of the deficiencies in the popular SPC/E and TIP3P models of water. *The Journal of Chemical Physics* **134**, 054106 (2011).

54. Pippig, M. & Mercuri, F. Efficient evaluation of Coulomb interactions in kinetic Monte Carlo simulations of charge transport. *The Journal of Chemical Physics* **152**, 164102 (2020).

55. Sousa da Silva, A.W. & Vranken, W.F. ACPYPE - AnteChamber PYthon Parser interfacE. *BMC Res Notes* **5**, 367 (2012).

56. M.J. Abraham, D.v.d.S., E. Lindahl, B. Hess, and the GROMACS development team (2019).

57. Bussi, G., Donadio, D. & Parrinello, M. Canonical sampling through velocity rescaling. *J Chem Phys* **126**, 014101 (2007).

58. Berendsen, H.J.C., Postma, J.P.M., van Gunsteren, W.F., DiNola, A. & Haak, J.R. Molecular dynamics with coupling to an external bath. *The Journal of Chemical Physics* **81**, 3684-3690 (1984).

59. Ryckaert, J.-P., Ciccotti, G. & Berendsen, H.J.C. Numerical integration of the cartesian equations of motion of a system with constraints: molecular dynamics of n-alkanes. *Journal of Computational Physics* **23**, 327-341 (1977).

60. Miyamoto, S. & Kollman, P.A. Settle: An analytical version of the SHAKE and RATTLE algorithm for rigid water models. *Journal of Computational Chemistry* **13**, 952-962 (1992).

61. Michaud-Agrawal, N., Denning, E.J., Woolf, T.B. & Beckstein, O. MDAnalysis: A toolkit for the analysis of molecular dynamics simulations. *Journal of Computational Chemistry* **32**, 2319-2327 (2011).

830 62. R Core Team (R Foundation for Statistical Computing, Vienna, Austria; 2017).
831 63. Chen, S., Burgner, J.W., Krahn, J.M., Smith, J.L. & Zalkin, H. Tryptophan fluorescence monitors
832 multiple conformational changes required for glutamine phosphoribosylpyrophosphate
833 amidotransferase interdomain signaling and catalysis. *Biochemistry* **38**, 11659-11669 (1999).
834

835 **Figure Legends**

836 **Figure 1. The yeast PPAT Ade4 concentrates in fine granules**

837 A. Bright field and GFP images of cells expressing Ade4 tagged C-terminally with the
838 indicated green fluorescent protein. Cells were grown in medium containing 0.02 mg/ml
839 adenine, washed with medium lacking adenine, and then incubated in medium without
840 adenine for 30 min before imaging. The intensity of GFP is represented by pseudo-colors
841 in the upper panels.

842 B. Quantification of the mean fluorescence intensity of Ade4 condensates observed in
843 cells as shown in (A). Data are represented by box and dot plots. Cross marks indicate
844 the population mean. *P* values versus mGFP are shown (Steel's multiple comparison test).

845 C. A higher resolution image of Ade4-mNG granules. Granules were imaged at an *xy*
846 resolution of 34 pixels/µm and z-spacing of 0.5 µm. Z-positions are represented by a color
847 code (left). A grayscale image of granules (middle) and bright field image of cells (right)
848 are also shown. Scale bar = 5 µm.

849 D. Time-lapse imaging of the assembly of Ade4-mNG granules by adenine depletion.
850 Cells were grown in medium containing 0.02 mg/ml adenine and washed with medium
851 lacking adenine at t = 0 min. Scale bar = 5 µm.

852 E. Time-lapse imaging of the disassembly of Ade4-mNG granules by adenine
853 supplementation. Cells were grown in the absence of adenine and 0.02 mg/ml adenine
854 was supplemented at t = 0 min. Scale bar = 5 µm.

855 F, G. Panels F and G show the quantification of data in (D) and (E), respectively. The
856 number of intracellular Ade4-mNG granules was counted as the number of maxima of
857 green fluorescence intensity per cell. Data are the mean over 10-12 independent fields of
858 view, and approximately 70 cells were examined per field. The shaded area indicates ±
859 1SD.

860 H. Schematic of *de novo* purine synthesis

861

862 **Figure 1S1. Additional data regarding the intracellular localization of Ade4. Related**
863 **to Figure 1**

864 A. Bright field and GFP images of cells expressing Ade4 tagged C-terminally with the
865 indicated green fluorescent protein. Cells were grown in medium containing 0.02 mg/ml
866 adenine and imaged.

867 B. Phase and RFP images of cells expressing Ade4 tagged C-terminally with the red
868 fluorescent protein mKate2. Scale bar = 5 µm.

869 C. A control experiment of time-lapse imaging of the assembly of Ade4-mNG granules
870 by adenine depletion shown in Fig. 1D. Cells were grown in medium containing 0.02

871 mg/ml adenine and washed with medium containing the same concentration of adenine
872 at t = 0 min. Scale bar = 5 μm.
873 D. A control experiment of time-lapse imaging of the disassembly of Ade4-mNG granules
874 by adenine supplementation shown in Fig. 1E. Cells were grown in the absence of adenine
875 and sterile water was supplemented in place of adenine at t = 0 min. Scale bar = 5 μm.
876
877 **Figure 2. Ade4 granules have liquid-like properties**
878 A. The aliphatic alcohol 1,6–hexanediol dissolves Ade4 granules. Cells harboring Ade4-
879 mNG granules in the absence of purine bases were treated with 2 μg/ml digitonin ± 10%
880 (w/v) 1,6-hexanediol for 10 min and then imaged. Scale bar = 5 μm.
881 B. Quantification of data shown in (A). The percentage of cells with Ade4-mNG granules
882 per field of view (containing 361 ± 159 cells) was plotted. Data were pooled from three
883 independent experiments. Bars and error bars indicate the mean ± 1SD. *P* values were
884 calculated using the two-tailed Steel-Dwass multiple comparison test.
885 C. Domain structure of the budding yeast Ade4. The bottom graph shows disorder
886 predictions by the DISOPRED algorithm.
887 D. The C-terminal IDR of Ade4 is required for granule assembly. Cells expressing the
888 mutant Ade4 lacking the C-terminal IDR tagged with mNG were incubated in the absence
889 of purine bases for 40 min and imaged.
890
891 **Figure 2S1. The C-terminal IDR is conserved in PPATs of Ascomycota**
892 Heatmap showing the disorder scores of PPAT amino acid sequences of 81 ascomycota.
893
894 **Figure 2S2. The IDR is conserved in PPATs of various species**
895 Heatmap showing the disorder scores of PPAT amino acid sequences of 100 organisms,
896 including 19 ascomycota. Phylogenetic groups are color-coded on the left.
897
898 **Figure 2S3. Amino acid sequences of IDRs vary across species**
899 A-B. Multiple amino acid sequence alignment of the C-terminal region of PPAT. In (A),
900 three fungi and 13 representative organisms from the following groups are selected:
901 archaea, bacteria, protozoa, plants, nematodes, insects, echinoidea, fish, amphibians,
902 mammals, reptiles, birds, and ascidians. In (B), 13 species are selected from ascomycota.
903
904 **Figure 3. Formation of Ade4 granules requires active TORC1 and ribosome**
905 **biogenesis**
906 A. Wild-type and *fpr1*Δ cells expressing Ade4-GFP were grown in medium containing

907 adenine and incubated in medium without adenine in the presence of 0.02% (v/v) DMSO
908 or 0.02% DMSO plus 2 μg/ml rapamycin for 30 min before imaging.
909 B. Rapamycin suppresses the assembly of Ade4-mNG granules. Wild-type cells
910 expressing Ade4-mNG were treated with rapamycin and imaged as described in (A).
911 C. Quantification of data shown in (B). The percentage of cells with Ade4-mNG granules
912 per field of view (containing 443 ± 138 cells) was plotted. Data were pooled from two
913 independent experiments. Bars and error bars indicate the mean ± 1SD. *P* values were
914 calculated using the two-tailed Mann-Whitney U test.
915 D. The assembly of Ade4-mNG granules was significantly suppressed in *sfp1*Δ and *sit4*Δ
916 cells.
917 E. Quantification of data shown in (C). The percentage of cells with Ade4-mNG granules
918 per field of view (containing 517 ± 123 cells) was plotted. Data were pooled from three
919 independent experiments. Bars and error bars indicate the mean ± 1SD. *P* values versus
920 wt were calculated using the two-tailed Steel's multiple comparison test.
921 F. The inhibition of ribosome synthesis suppresses the assembly of Ade4 condensates.
922 Cells expressing Ade4-GFP were grown in medium containing adenine and then
923 incubated in medium without adenine in the presence of 0.05% (v/v) DMSO or 0.05%
924 DMSO plus 5 μg/ml diazaborine for 30 min before imaging. The percentage of cells with
925 Ade4-GFP foci per field of view (containing 780 ± 214 cells) was plotted. Data were
926 pooled from two independent experiments. Bars and error bars indicate the mean ± 1SD.
927 *P* values were calculated using the two-tailed Mann-Whitney U test. Representative cell
928 images are shown in Figure 3S1C. Scale bar = 5 μm.
929
930 **Figure 3S1. Formation of Ade4 granules in TORC1-related mutants. Related to**
931 **Figure 3.**
932 A. Assembly of Ade4-GFP foci in single gene deletion mutants of the upstream regulator
933 and downstream effector of TORC1 signaling. Cells of the indicated genotype expressing
934 Ade4-GFP were grown in medium containing adenine and then incubated in medium
935 without adenine for 30 min before imaging.
936 B. Summary of the percentage of cells showing Ade4-GFP foci in the wild-type and 37
937 single-gene deletion mutants. The percentage of cells with Ade4-GFP foci per field of
938 view was plotted. Data were pooled from 2-3 independent experiments. Bars and error
939 bars indicate the mean ± 1SD.
940 C. The inhibition of ribosome synthesis suppressed the assembly of Ade4-GFP foci.
941 Related to Figure 3F.
942 D. The inhibition of ribosome synthesis suppressed the assembly of Ade4-mNG granules.

943 Cells expressing Ade4-mNG were grown in medium containing adenine and then
944 incubated in medium without adenine in the presence of 0.05% (v/v) DMSO or 0.05%
945 DMSO plus 5 μg/ml diazaborine for 30 min before imaging. Scale bar = 5 μm.
946
947 **Figure 4. Intracellular derivatives of purine nucleotides prevent the formation of**
948 **Ade4 condensates**
949 A. *De novo* and salvage pathways for purine synthesis in budding yeast.
950 B. Assembly of Ade4-GFP foci in purine metabolism mutants. Cells having Ade4-GFP
951 foci in the absence of purine bases (mock) were treated with the same medium or medium
952 containing 20 μg/adenine (+adenine) or 25 μg/ml hypoxanthine (+hypoxanthine) for 20
953 min and then imaged. Scale bar = 5 μm.
954 C-E. Quantification of data shown in (B). The percentage of cells with foci per field of
955 view was quantified and plotted. Bars and error bars indicate the mean ± 1SD. Data were
956 pooled from 2-3 independent experiments, and more than 16 fields of view were imaged
957 for each condition. Triple asterisks indicate *p* values less than 10^{-10} versus the mock
958 (Steel's multiple comparison test, two-tailed). The single asterisk indicates a *p* value less
959 than 0.01 versus the mock. NS, not significant (*p* value >0.05).
960
961 **Figure 4S1. Alanosine inhibits the dissolution of Ade4 foci in the presence of**
962 **hypoxanthine. Related to Figure 4.**
963 A. Alanosine inhibits the adenylosuccinate synthetase ADE12.
964 B. Assembly of Ade4-GFP foci in the presence of alanosine. Cells expressing Ade4-GFP
965 were incubated in medium lacking adenine in the presence of 0 (mock) or 30 μg/ml
966 alanosine (+alanosine) for 40 min to allow the assembly of Ade4-GFP foci and were then
967 imaged (SC). Cells were further treated with the same medium supplemented with 24
968 μg/ml hypoxanthine for 15 min and then imaged again (SC + hyp). Scale bar = 5 μm.
969 C. Quantification of data shown in (B). The percentage of cells with foci per field of view
970 (containing 182 ± 46 cells) was quantified and plotted. Data were pooled from two
971 independent experiments. Bars and error bars indicate the mean ± 1SD. The significance
972 of differences was tested using the unpaired one-tailed Welch's *t*-test. *P* values versus the
973 mock are shown.
974
975 **Figure 5. The interaction of purine nucleotides with Ade4 is implicated in granule**
976 **assembly**
977 A. Interaction between ADP and specific amino acid residues in *B. subtilis* PPAT (pdb
978 file: 1ao0). The dotted line indicates a hydrogen bond.

979 B. Amino acid residues involved in the interaction with purine nucleotides are well
980 conserved among species.
981 C-E. Examination of the Ade4-VQQ mutant. Ade4-mNG and Ade4-VQQ-mNG cells
982 were incubated in medium without purine bases for 40 min to allow for the assembly of
983 Ade4 granules and then imaged. The percentage of cells with granules per field of view
984 (containing 265 ± 80 cells) was quantified and plotted in (C). The number of granules
985 detected in the cell were averaged over the field of view and plotted in (D). The mean
986 fluorescence intensity of granules was box plotted in (E). Data were pooled from three
987 independent experiments. Bars and error bars indicate the mean ± 1SD. The significance
988 of differences was tested using the unpaired two-tailed Welch's *t*-test (C) or Mann-
989 Whitney U test (D, E). *P* values versus wt are shown.
990
991 **Figure 6. The Ade4 protein condensates into particles under molecular crowding**
992 **conditions *in vitro***
993 A. Pure Ade4-mNG condensated into fine particles in a PEG concentration-dependent
994 manner. Following the supplementation of 0.15 μM Ade4-mNG with PEG8000 at the
995 indicated concentration (%, w/v), images were taken after a 1-min incubation. Inverted
996 grayscale images are shown. Scale bar = 5 μm.
997 B-C. Quantification of data shown in (A). The mean fluorescence intensities of Ade4-
998 mNG particles were box plotted in (B). Cross marks indicate the population mean. The
999 integrated fluorescence intensities of particles were summed per field and plotted in (C).
1000 Bars and error bars indicate the mean ± 1SD. Seven to 10 fields of view were imaged for
1001 each condition and an average of 390 particles per field were examined.
1002 D. 1,6-Hexanediol attenuated the *in vitro* condensation of Ade4-mNG. Following the
1003 supplementation of 0.15 μM Ade4-mNG with 10% PEG8000 in the presence of 0 or 10%
1004 (w/v) 1,6-hexanediol, images were taken after a 1-min incubation. Fluorescence intensity
1005 is represented by pseudo-colors. Scale bar = 5 μm.
1006 E-F. Quantification of data shown in (D). The mean fluorescence intensities of particles
1007 were box plotted in (E). Cross marks indicate the population mean. The integrated
1008 fluorescence intensities of particles were summed per field and plotted in (F). Bars and
1009 error bars indicate the mean ± 1SD. Ten fields of view were imaged for each condition,
1010 and an average of 1197 particles per field were examined. *P* values were calculated using
1011 the two-tailed Mann-Whitney U test (E) or Welch's *t*-test (F).
1012 G. Ade4ΔIDR-mNG assembled into granules less effectively than Ade4-mNG *in vitro*.
1013 Following the supplementation of 0.2 μM Ade4-mNG or Ade4ΔIDR-mNG with 10%
1014 PEG8000, images were taken after a 1-min incubation. Fluorescence intensity is

represented by pseudo-colors. Scale bar = 5 μm.

H-I. Quantification of data shown in (G). The mean fluorescence intensities of particles were box plotted in (H). Cross marks indicate the population mean. The integrated fluorescence intensities of particles were summed per field and plotted in (I). Bars and error bars indicate the mean ± 1SD. Twenty-eight fields of view were imaged for each condition, and an average of 1341 particles per field were examined. *P* values were calculated using the two-tailed Mann-Whitney U test.

Figure 6S1. Purification and basic characterization of the Ade4 protein *in vitro*

A. Purified proteins used in the present study. Proteins were resolved by SDS-PAGE and stained with FastGene™ Q-stain.

B. The pure mNG protein did not condensate into particles even under molecular crowding conditions. Following the supplementation of 0.14 μM mNG with 0 or 10% PEG8000, images were taken after a 1-min incubation. Scale bar = 5 μm.

C. The *in vitro* condensation of Ade4-mNG depends on the size of PEG. Following the supplementation of 0.15 μM Ade4-mNG with 10% PEG of the indicated average molecular weight, images were taken after a 1-min incubation. Scale bar = 5 μm.

D-E. Quantification of data shown in (C). The mean fluorescence intensities of Ade4-mNG particles were box plotted in (D). Cross marks indicate the population mean. The integrated fluorescence intensities of particles were summed per field and plotted in (E). Bars and error bars indicate the mean ± 1SD. Seven to 8 fields of view were imaged for each condition, and an average of 399 particles per field were examined.

F. Condensation of Ade4-mNG into particles with crowding agents other than PEG. Between 0.13 and 0.14 μM Ade4-mNG was supplemented with the indicated crowding agents and images were taken after a 1-min incubation. Scale bar = 5 μm.

Figure 6S2. Estimation of the intracellular concentration of Ade4.

Data regarding the protein abundance of the budding yeast Ade4 were downloaded from the Saccharomyces Genome Database (https://www.yeastgenome.org/locus/S000004915/protein). Data were derived from twenty quantitative genome-wide proteomic studies and normalized to a unit of molecules per cell. These values were converted to micromoles assuming that the average cytoplasmic volume of the haploid yeast cell is 42 fℓ (Jorgensen et al., 2002). Data were classified according to the condition of cells (unstressed or stressed), measuring methods (flow cytometry, quantitative fluorescence microscopy, and immunoblotting), and the type of medium (rich or synthetic) and then plotted. Bars and error bars indicate the mean

1051 ± 1SD.
1052
1053 **Figure 7. Purine nucleotides attenuate the assembly of Ade4 particles *in vitro***
1054 A. Effects of purine nucleotides on the *in vitro* assembly of Ade4 particles. Following the
1055 supplementation of 0.2 μM Ade4-mNG with 10% PEG8000 in the presence of the
1056 indicated purine nucleotide, images were taken after a 2-min incubation. The integrated
1057 fluorescence intensities of particles were summed per field and plotted. Bars and error
1058 bars indicate the mean ± 1SD. Between 23 and 28 fields of view were imaged for each
1059 condition from two independent preparations, and an average of 1323 particles per field
1060 were examined. *P* values were calculated using the two-tailed Tukey-Kramer's multiple
1061 comparison test. ***, $p < 0.001$; NS, not significant (p value > 0.05).
1062 B-D. The supplementation of 0.2 μM Ade4-mNG with 10% PEG8000 was performed in
1063 the presence of the indicated concentration of AMP (B), ADP (C), and ATP (D). The
1064 integrated fluorescence intensities of particles were summed per field, normalized to the
1065 mean at 0 μM, and plotted. Bars and error bars indicate the mean ± 1SD. Between 28 and
1066 55 fields of view were imaged for each condition from 2 or 3 independent preparations,
1067 and an average of 1200 particles per field were examined.
1068 E. Effects of AMP on the *in vitro* assembly of Ade4 and Ade4ΔIDR particles. The
1069 supplementation of 0.2 μM Ade4-mNG (FL) or Ade4ΔIDR-mNG (ΔIDR) with 10%
1070 PEG8000 was performed in the presence of 0 or 500 μM AMP. The integrated
1071 fluorescence intensities of particles were summed per field, normalized to the mean of
1072 FL at 0 μM AMP, and plotted. Bars and error bars indicate the mean ± 1SD. Between 40
1073 and 45 fields of view were imaged for each condition from 3 independent preparations.
1074 *P* values were calculated using the two-tailed Welch's *t*-test.
1075 F. Schematic model showing the regulation of Ade4 condensation proposed in the present
1076 study. See the text for details.
1077
1078 **Figure 7S1. Additional data regarding the assembly of Ade4 particles *in vitro*, related**
1079 **to Fig. 7.**
1080 A, B. Effects of purine base derivatives on the *in vitro* assembly of Ade4 particles.
1081 Following the supplementation of 0.2 μM Ade4-mNG with 10% PEG8000 in the
1082 presence of the indicated compound, images were taken after a 2-min incubation. Glucose
1083 was used as a negative control. The integrated fluorescence intensities of particles were
1084 summed per field and plotted in (A). The mean fluorescence intensities of Ade4-mNG
1085 particles were averaged per field and plotted in (B). Bars and error bars indicate the mean
1086 ± 1SD. Twenty fields of view were imaged for each condition from two independent

1087 preparations, and an average of 1452 particles per field were examined. *P* values were
1088 calculated using the two-tailed Steel's multiple comparison test. NS, not significant (*p*
1089 value >0.05).
1090 C. Effects of purine nucleotides on the *in vitro* assembly of Ade4 particles. Data were
1091 from the same experiment shown in Figure 7A. The mean fluorescence intensities of
1092 Ade4-mNG particles were averaged per field and plotted. Bars and error bars indicate the
1093 mean ± 1SD. *P* values were calculated using the two-tailed Tukey-Kramer's multiple
1094 comparison test. ***, $p < 0.001$; NS, not significant (*p* value >0.05).
1095 D. The supplementation of 0.2 μM Ade4-mNG with 10% PEG8000 was performed in the
1096 presence of the indicated concentration of GMP. The integrated fluorescence intensities
1097 of particles were summed per field, normalized to the mean at 0 μM, and plotted. Bars
1098 and error bars indicate the mean ± 1SD. Between 25 and 30 fields of view were imaged
1099 for each condition from two independent preparations, and an average of 1200 particles
1100 per field were examined.
1101
1102 **Figure 8. The formation of Ade4 granules is important for efficient *de novo* purine**
1103 **synthesis during cell growth**
1104 A. Growth of ADE4-3HA and ADE4ΔIDR-3HA cells on solid media. Cells of each strain
1105 were serially diluted (five-fold), spotted on 2% glucose medium containing the indicated
1106 nitrogen source, and then grown at 30°C for 2-3 days.
1107 B. Immunoblot analysis of the protein level of Ade4. Total cell extracts were prepared
1108 from cells expressing the indicated Ade4 construct. Ade4-3HA and Ade4ΔIDR-3HA were
1109 detected as approximately 60-kDa bands by an anti-HA antibody. The bands of GAPDH
1110 were shown as a loading control.
1111 C. Growth curves of Ade4-3HA and Ade4ΔIDR-3HA cells in liquid media without
1112 adenine. Cells were grown at 30°C for 40 h in medium containing the indicated nitrogen
1113 source in the absence of adenine. Data are the mean of 6 replicates, and the shaded area
1114 indicates ± 1SD.
1115 D. Quantification of data shown in (C). The time to half-maximum density
1116 (corresponding to normalized OD_{595} = 0.5) was calculated and plotted. Bars and error
1117 bars indicate the mean ± 1SD. *P* values were calculated using the two-tailed Welch's *t*-
1118 test.
1119
1120 **Figure 8S1. Cell growth assay in the presence of external purine bases, related to Fig.**
1121 **8.**
1122 A. Growth curves of Ade4-3HA and Ade4ΔIDR-3HA cells in liquid media containing

1123 adenine. Cells were grown at 30°C for 40 h in medium containing the indicated nitrogen
1124 source in the presence of adenine. Data are the mean of 6 replicates, and the shaded area
1125 indicates ± 1SD.
1126 B. Quantification of data shown in (A). The time to half-maximum density
1127 (corresponding to normalized OD_{595} = 0.5) was calculated and plotted. Bars and error
1128 bars indicate the mean ± 1SD. *P* values were calculated using the two-tailed Welch's *t*-
1129 test.
1130 C. Reaction formulae corresponding to the glutamine-dependent PRA synthesis (Gln-
1131 PRA activity) and NH_3-dependent PRA synthesis (NH_3-PRA activity) of PPAT.
1132 D. Relationship between ammonia concentrations and the two activities of PPAT.
1133
1134 **Figure 9. MD calculations predict the potential leakage of glutamine-derived NH_3**
1135 **from PPAT molecules**
1136 (A-C) Time series for the dihedral angle of the Phe260 side chain and the distance of NH_3
1137 from the initial structure (A: holo; B: semi-holo; and C: R333A mutant). Moving averages
1138 are plotted in bold lines. Under each condition, 100-ns simulations were performed ten
1139 times individually. The blue backgrounds indicate the open state of the Phe260 sidechain.
1140 (D) The hydrophobic (orange) and front (red) channels of *E. coli* PPAT. (E) A structural
1141 snapshot around the Arg gate. Hydrogen bonds are shown as red dotted lines. (F) The
1142 reaction mechanism suggested in a previous study. (G) The reaction mechanism
1143 suggested in the present study. (H) Intramolecular and intermolecular channeling of NH_3.
1144
1145 **Figure 9S1. Possible enzymatic reaction pathways of PPAT**
1146 A. Intramolecular channeling of glutamine-derived NH_3 proposed by Krahn et al.[39].
1147 B. Mechanism of NH_3-dependent activity proposed by Chen et al.[63]. External NH_3 enters
1148 the channel from the glutamine site irrespective of glutamine binding.
1149 C. The MD simulation in the present study suggests that glutamine-derived NH_3 leaks
1150 through the front channel following the attack of exogenous NH_3.
1151 D. Condensation-dependent activation of Ade4 proposed by the present study. Glutamine-
1152 derived NH_3 leaked from the front channel rapidly diffuses away. In the Ade4 condensate,
1153 the opportunity for NH_3 to be captured by other molecules and further reacted with PRPP
1154 will increase. This activation may be described as intermolecular NH_3 channeling. PRPP
1155 is not depicted in the schema.

Supplemental Information

Captions for supplementary movies

Movie S1

Time-lapse imaging of the assembly of Ade4-mNG granules by adenine depletion. Cells were grown in medium containing 0.02 mg/ml adenine and washed with medium lacking adenine at t = 0 min. The three cells in the upper right are shown in Fig. 1D. Scale bar = 5 µm.

Movie S2

Another example of cells showing the assembly of Ade4-mNG granules by adenine depletion. Experimental conditions are the same as in Movie S1. Scale bar = 5 µm.

Movie S3

A control experiment of time-lapse imaging of the assembly of Ade4-mNG granules by adenine depletion. Cells were grown in medium containing 0.02 mg/ml adenine and washed with medium containing the same concentration of adenine at t = 0 min. The rightmost cell is shown in Fig. 1S1C. Scale bar = 5 µm.

Movie S4

Time-lapse imaging of the disassembly of Ade4-mNG granules by adenine supplementation. Cells were grown in the absence of adenine and 0.02 mg/ml adenine was supplemented at t = 0 min. The four cells in the upper left are shown in Fig. 1E. Scale bar = 5 µm.

Movie S5

A control experiment of time-lapse imaging of the disassembly of Ade4-mNG granules by adenine supplementation. Cells were grown in the absence of adenine and sterile water was supplemented in place of adenine at t = 0 min. The two cells in the center are shown in Fig. 1S1D. Scale bar = 5 µm.

Movie S6

Another example of cells showing Ade4-mNG granules after a mock treatment with adenine. Experimental conditions are the same as in Movie S5. Scale bar = 5 µm.

Figure 1: The yeast PPAT Ade4 concentrates in fine granules

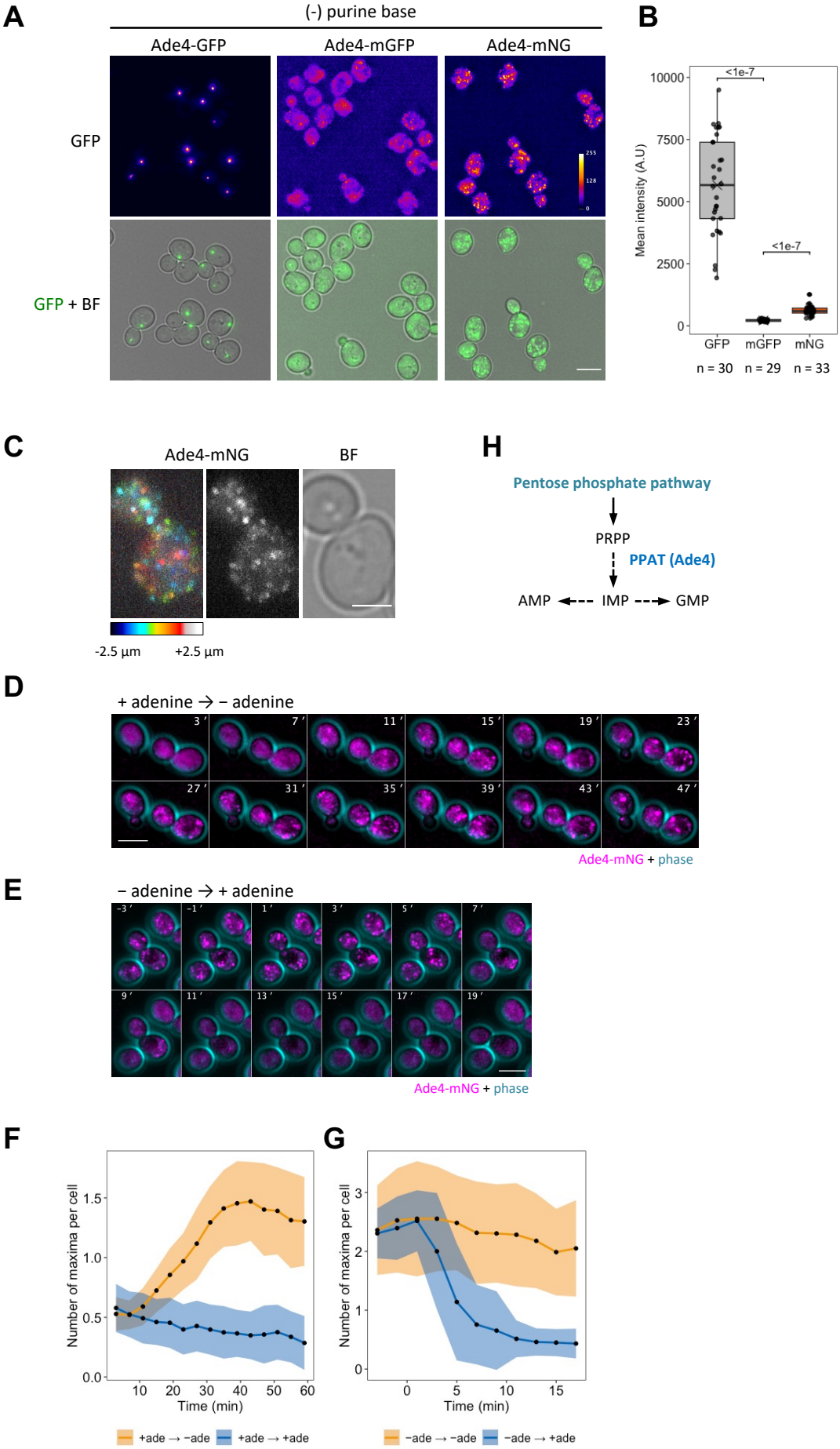

Figure 1S1: Additional data regarding the intracellular localization of Ade4. Related to Figure 1

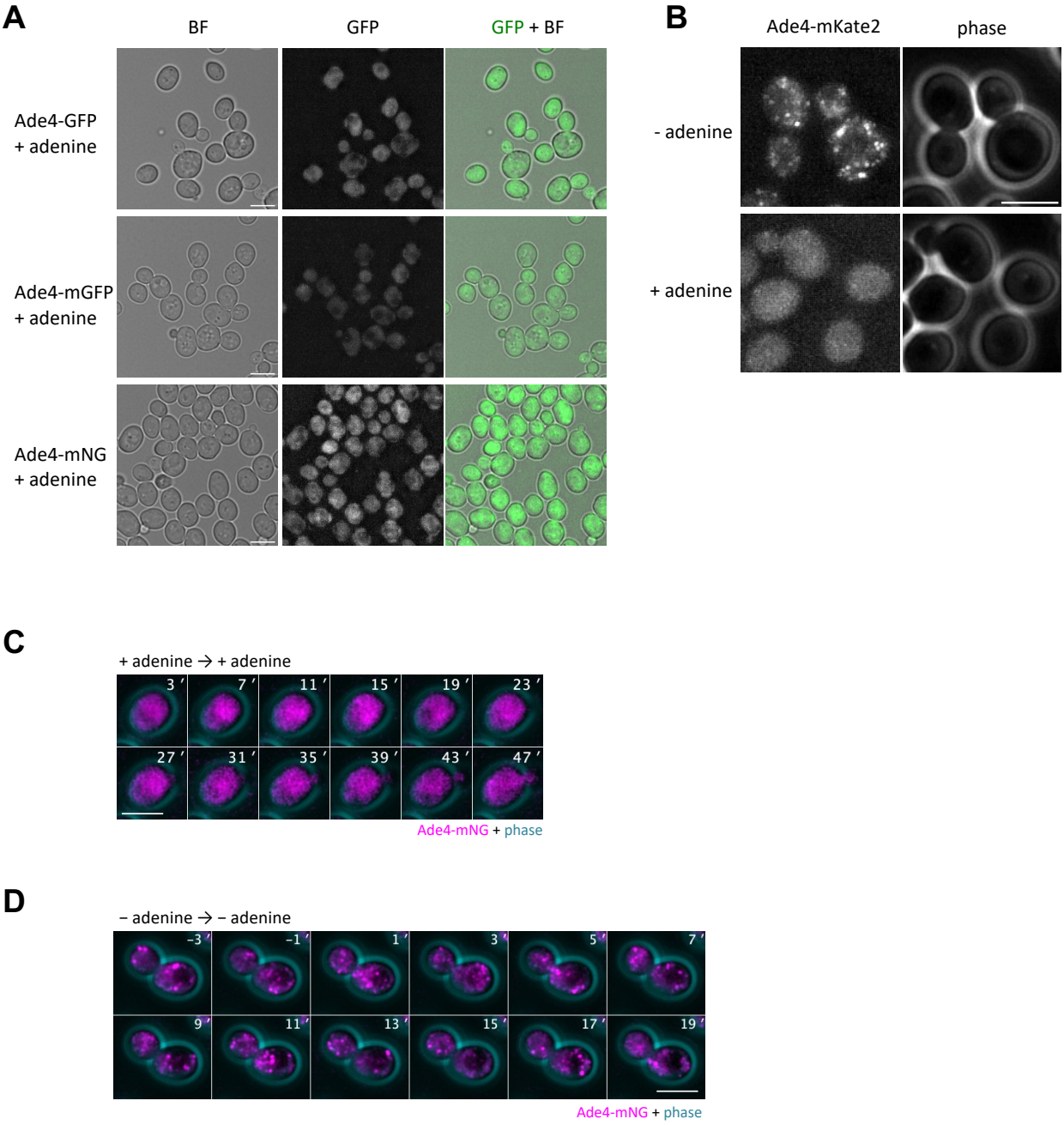

Figure 2: Ade4 granules have liquid-like properties

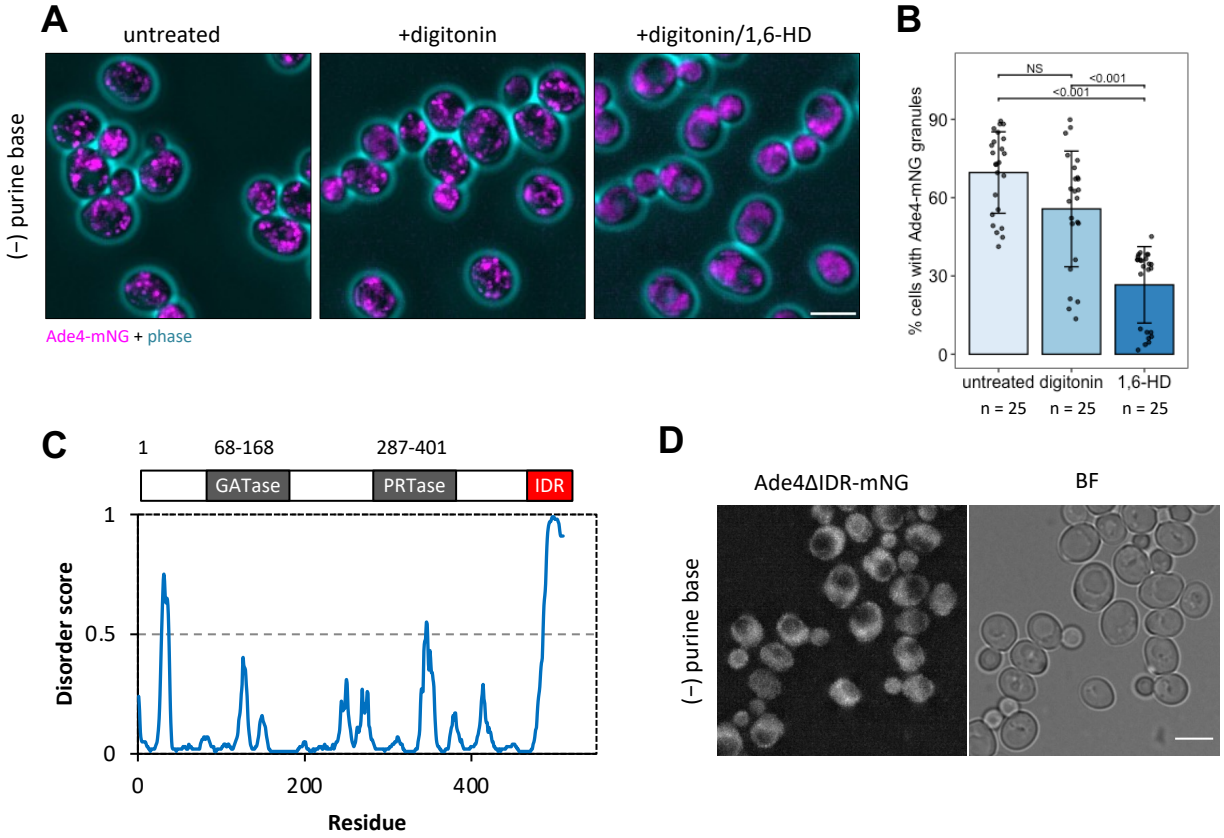

Figure 2S1: The C-terminal IDR is conserved in PPATs of Ascomycota

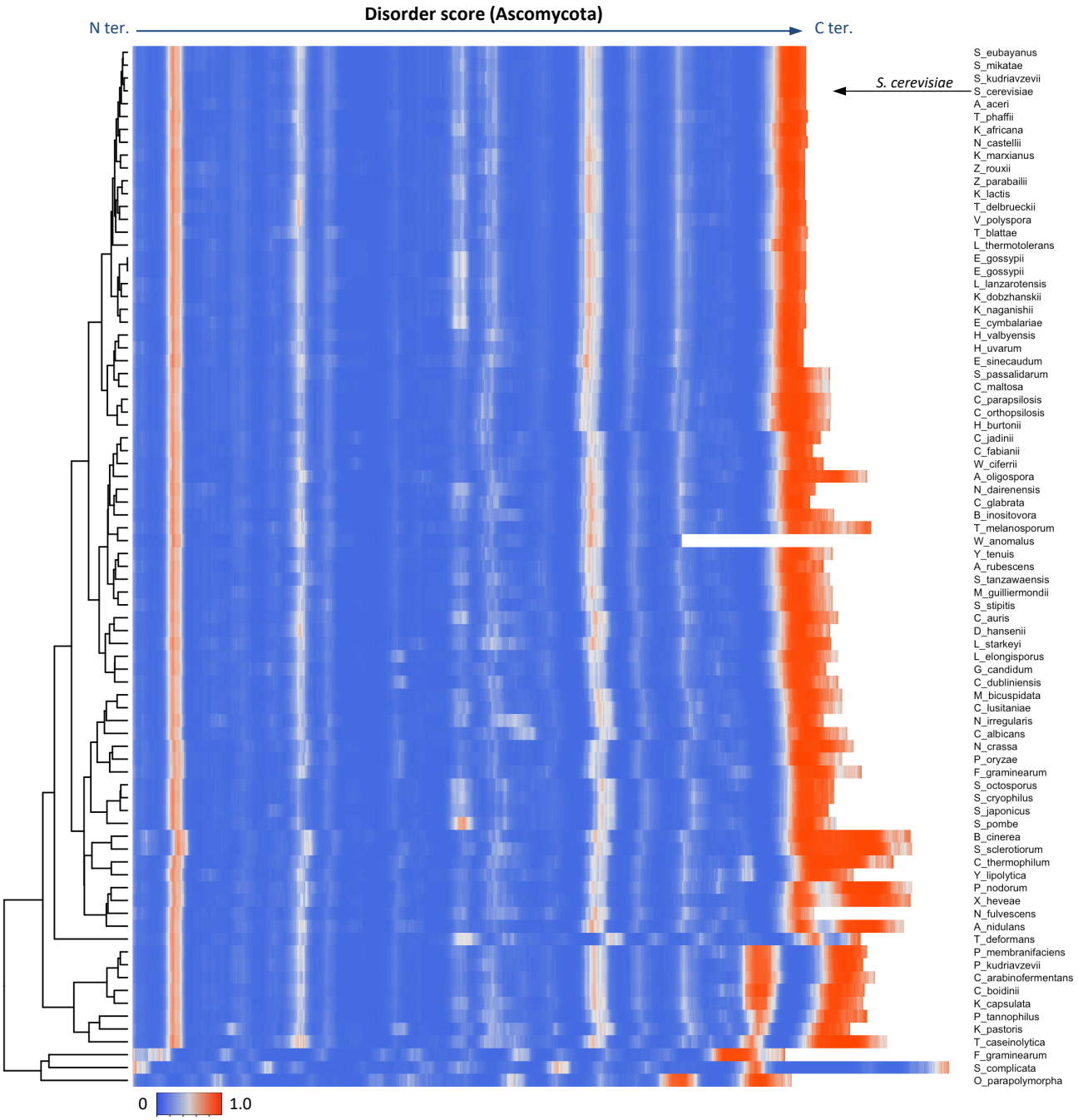

Figure 2S2: The IDR is conserved in PPATs of various species

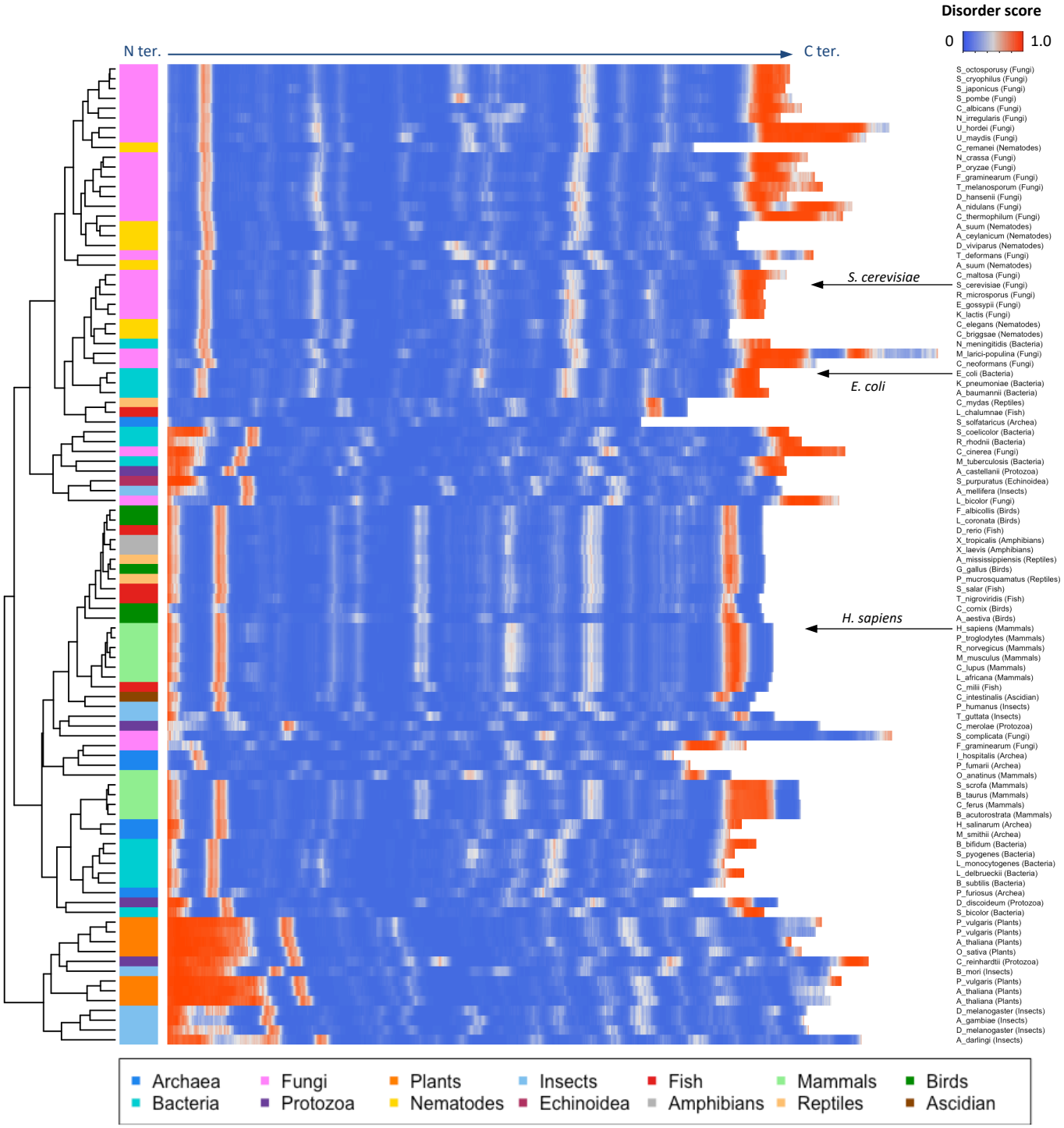

Figure 2S3: Amino acid sequences of IDRs vary across species

A

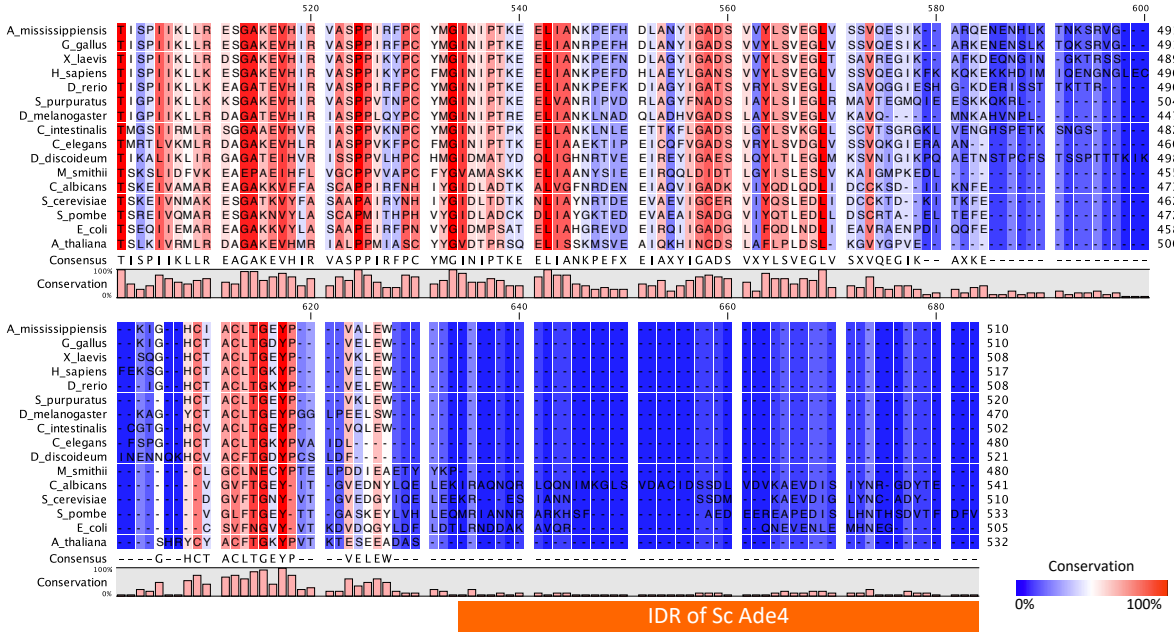

B

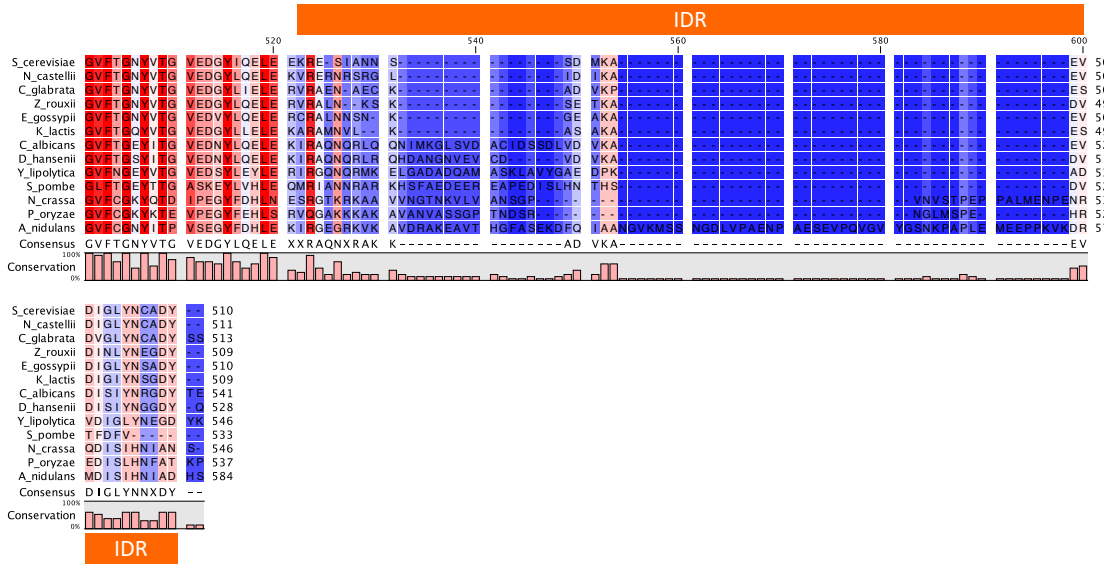

Figure 3: Formation of Ade4 granules requires active TORC1 and ribosome biogenesis

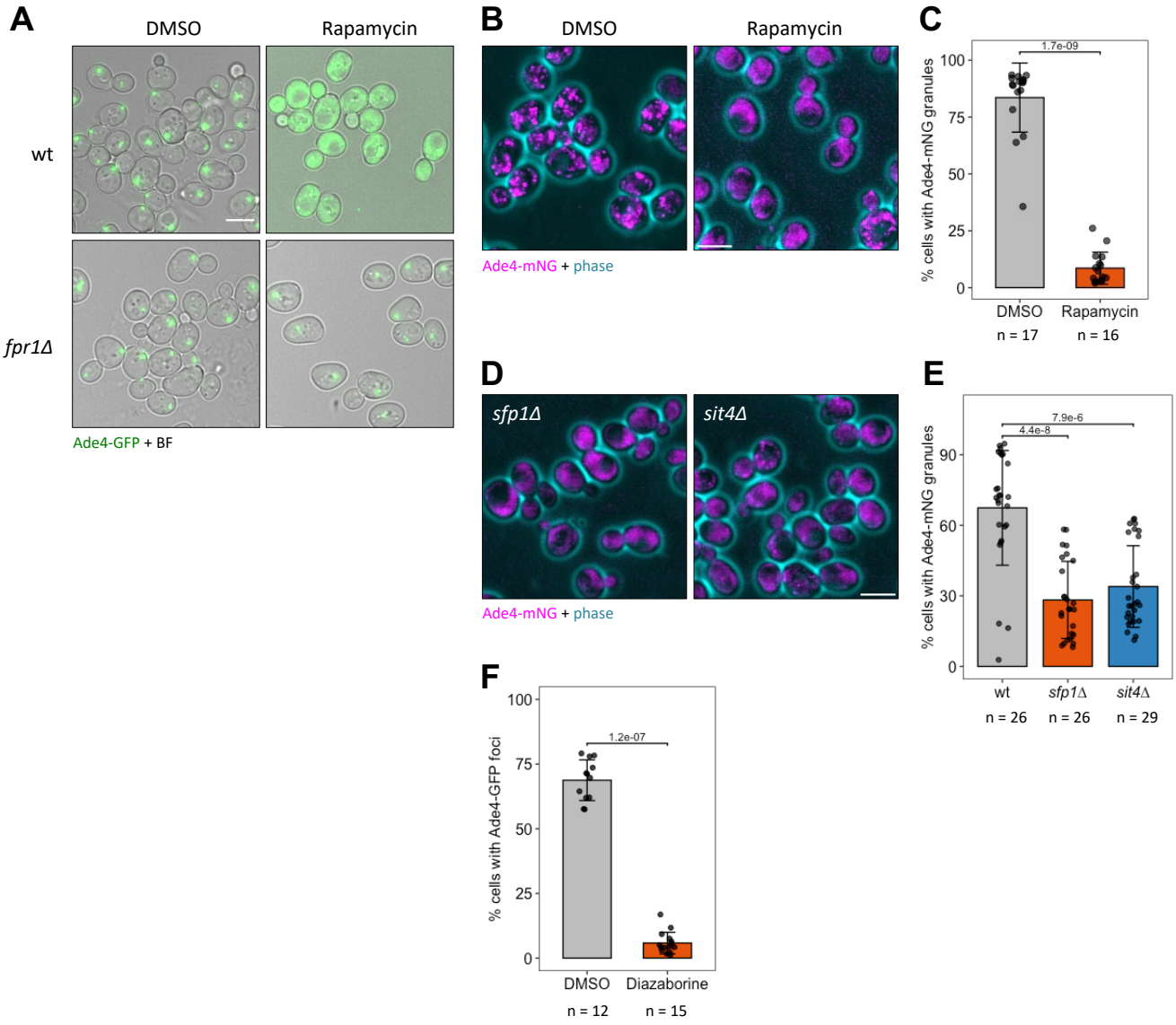

Figure 3S1: Formation of Ade4 granules in TORC1-related mutants. Related to Figure 3

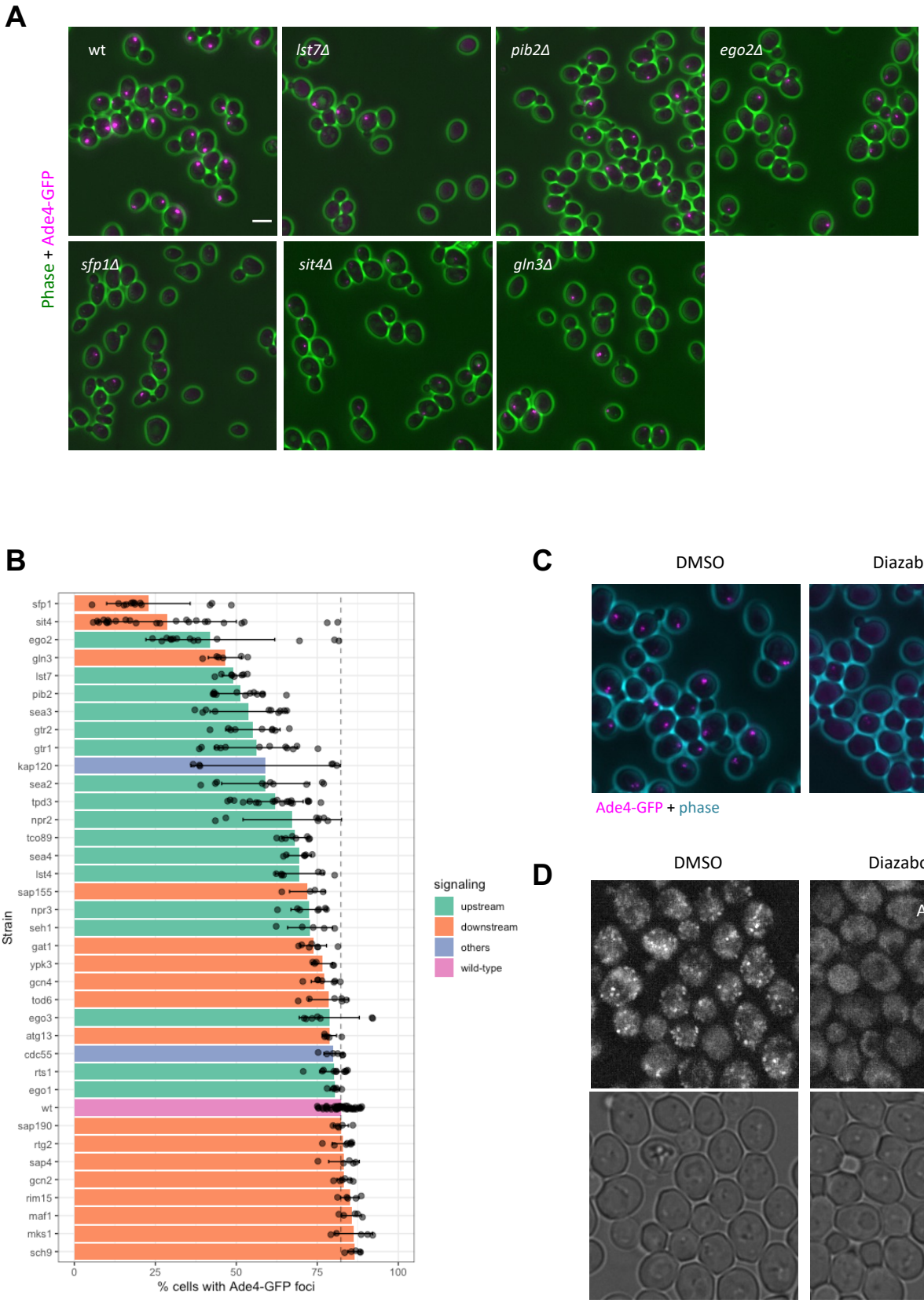

Figure 4: Intracellular derivatives of purine nucleotidse prevent the formation of the Ade4 condensates

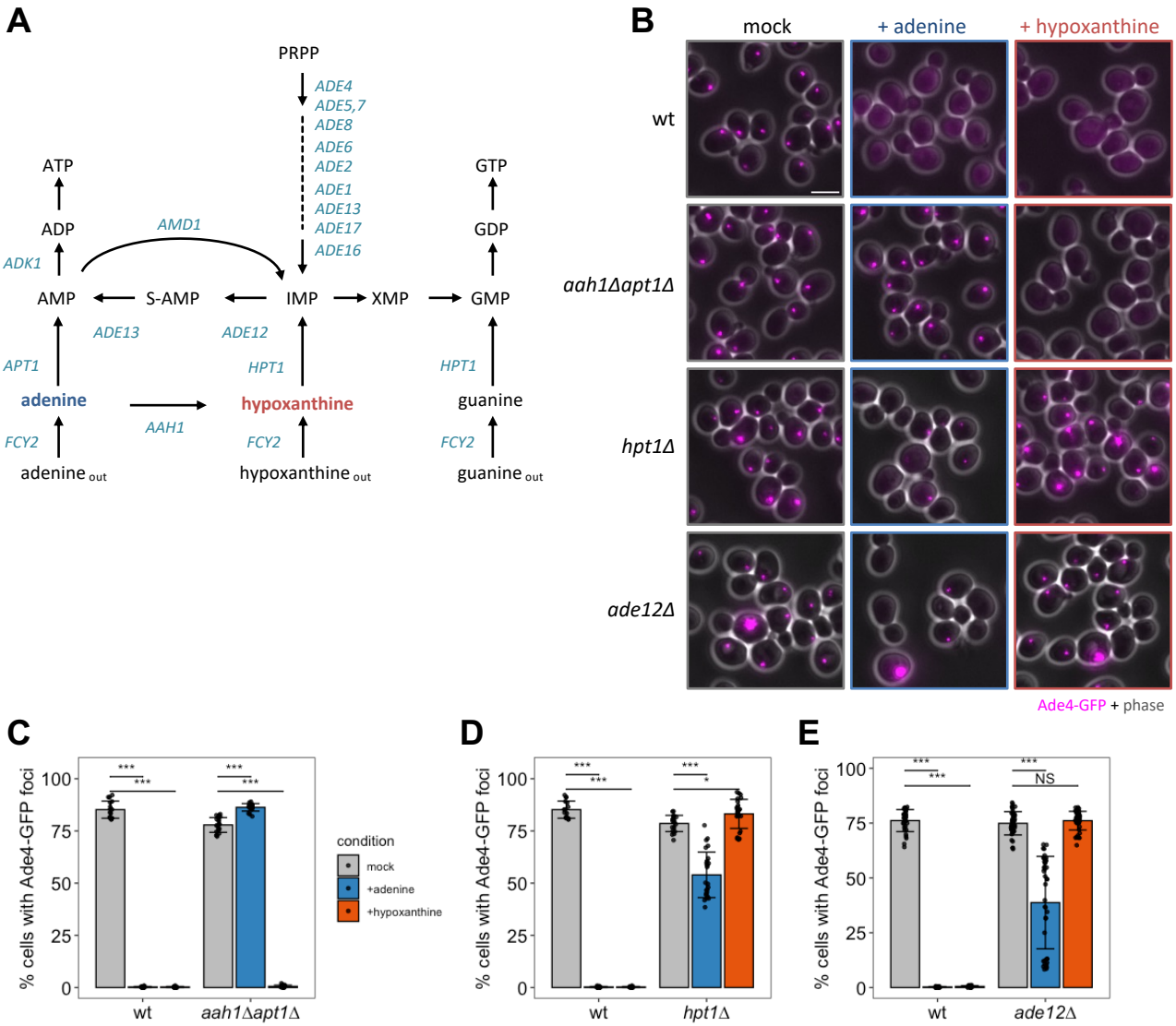

Figure 4S1: Alanosine inhibits the dissolution of the Ade4 foci in the presence of hypoxanthine

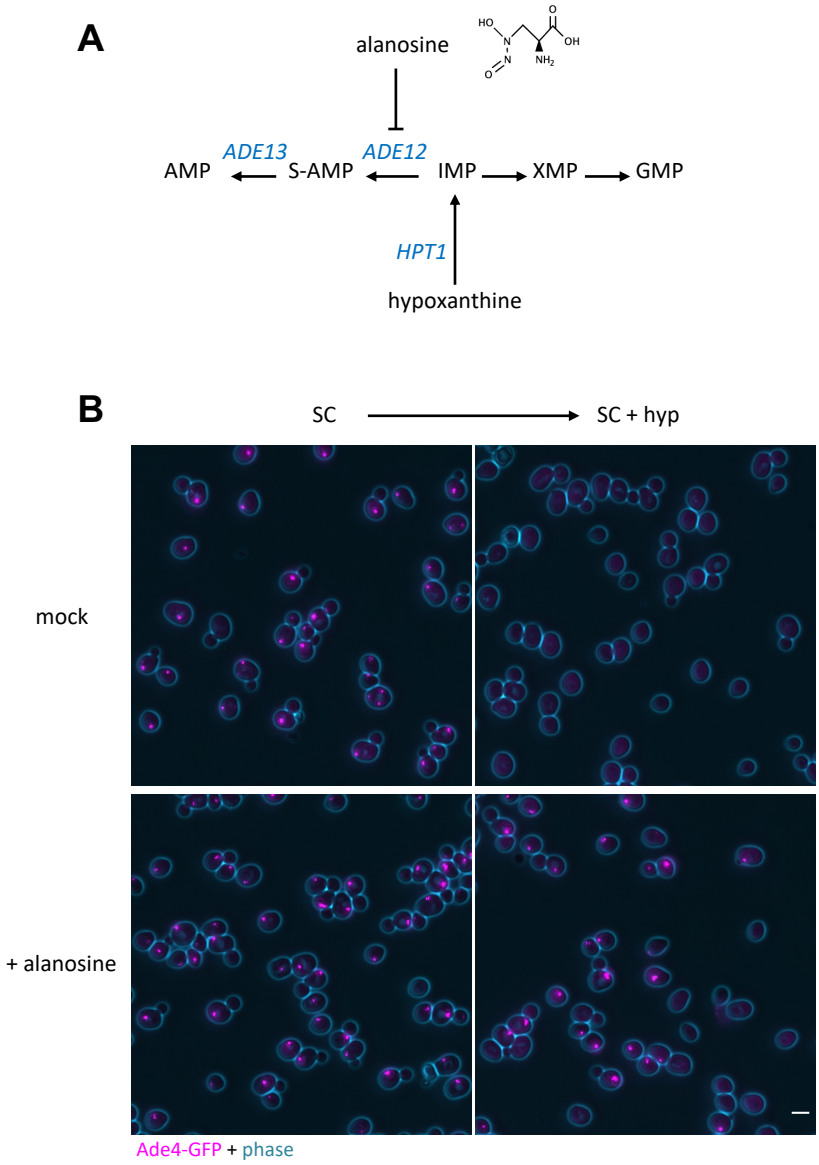

Figure 5: The interaction of purine nucleotides with Ade4 is implicated in the granule assembly

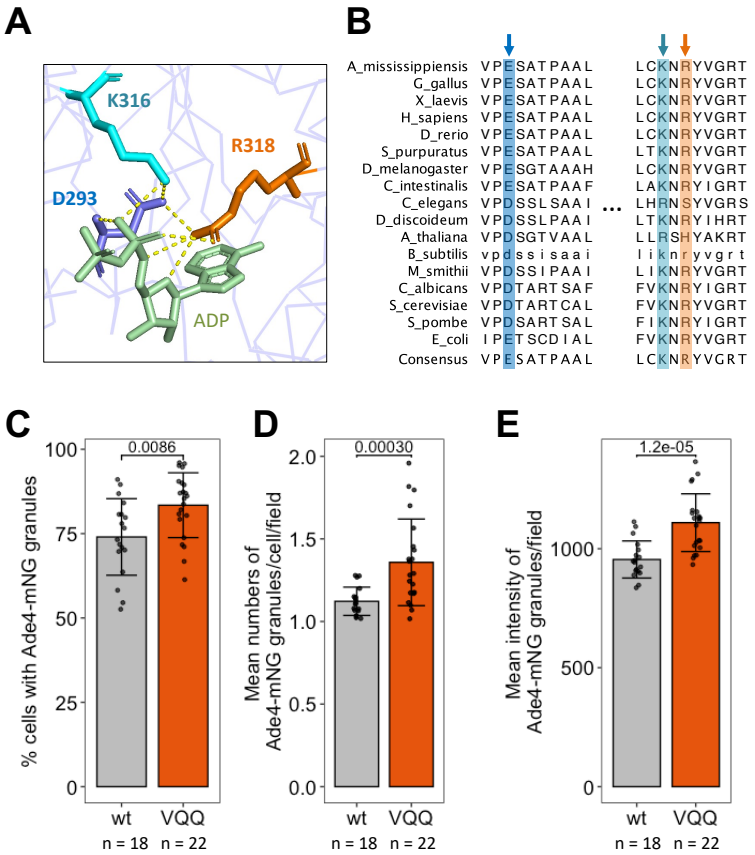

Figure 6: The Ade4 protein condensates into particles under molecular crowding conditions *in vitro*

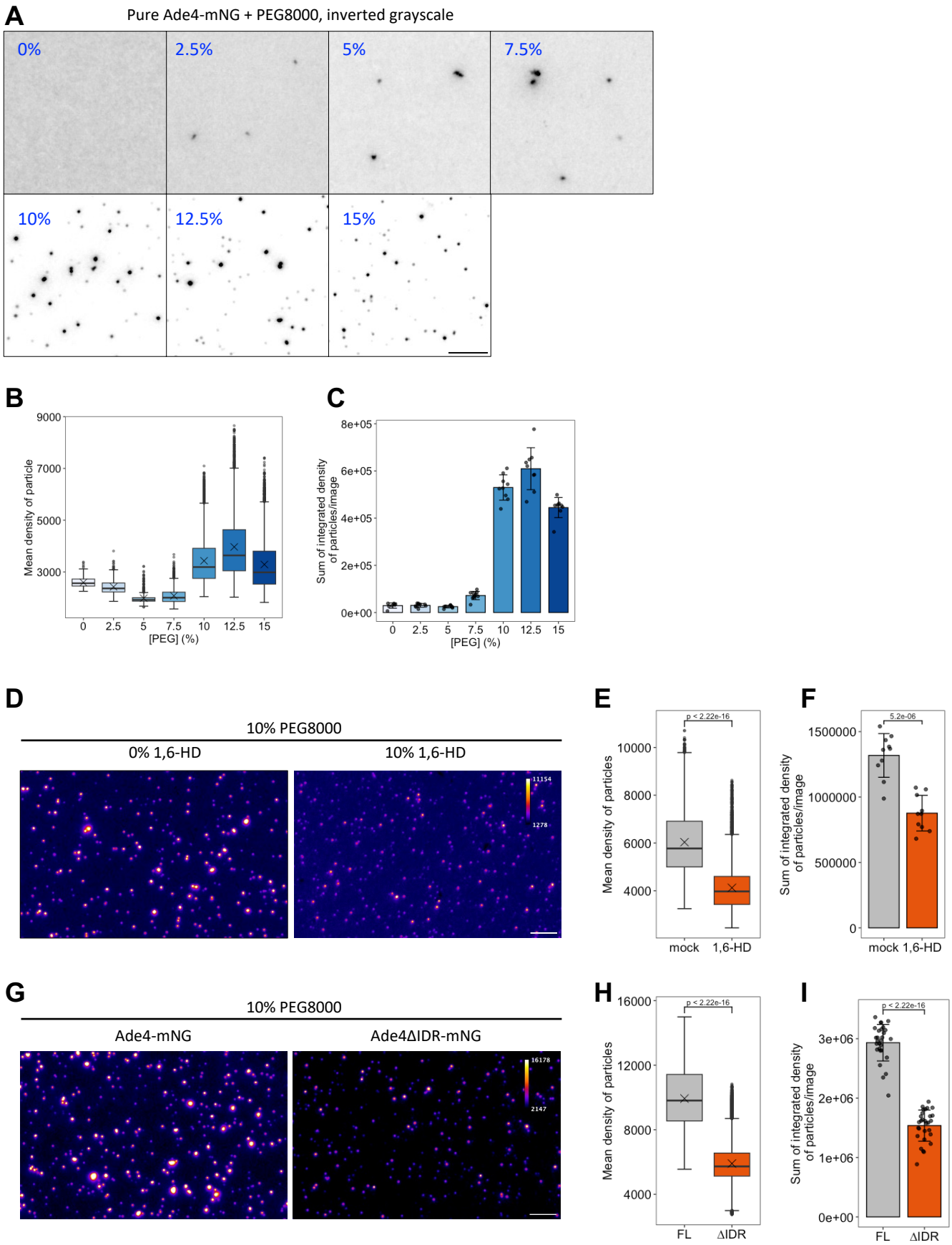

Figure 6S1: Purification and basic characterization of the Ade4 protein *in vitro*

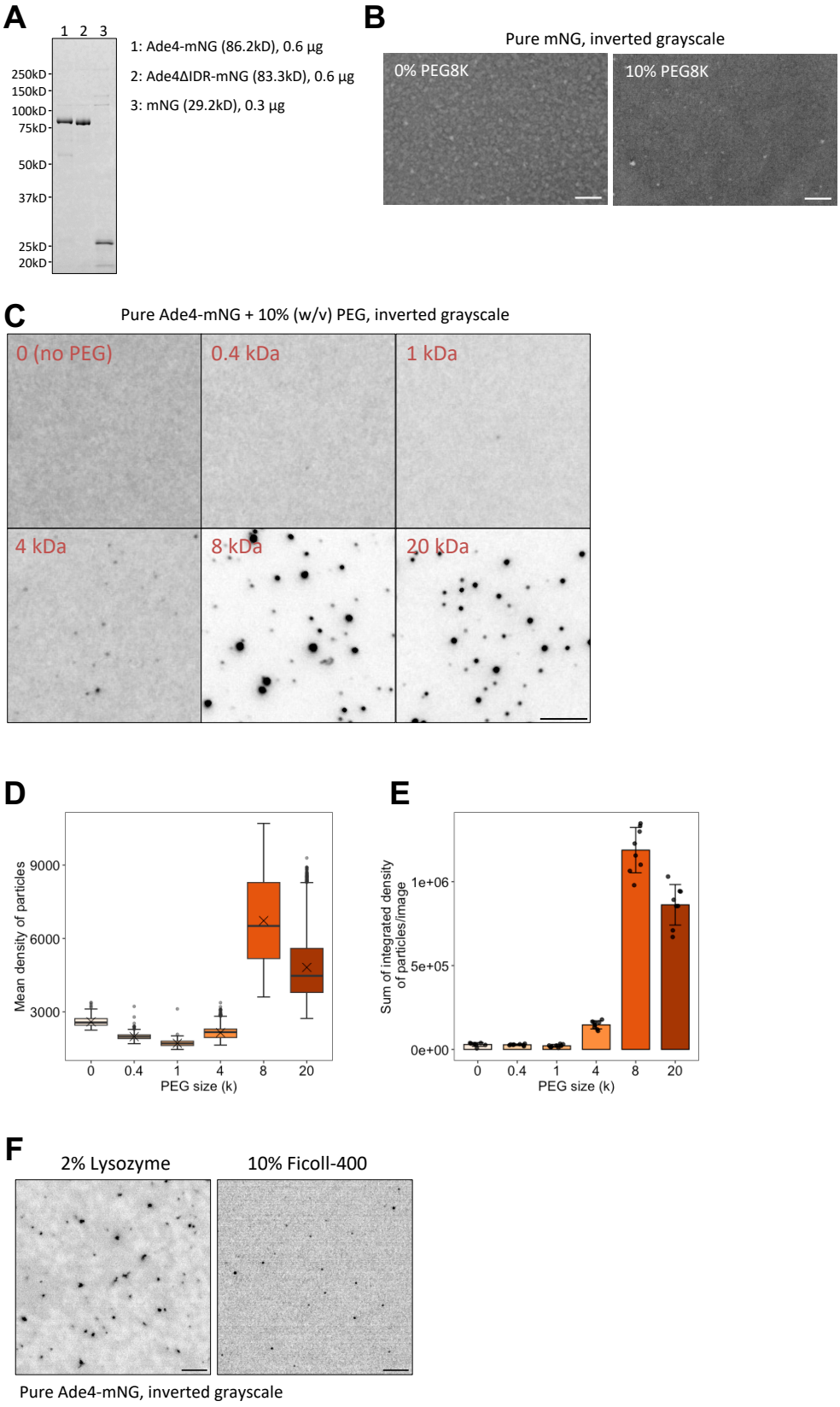

Figure 6S2: Estimation of the intracellular concentration of Ade4

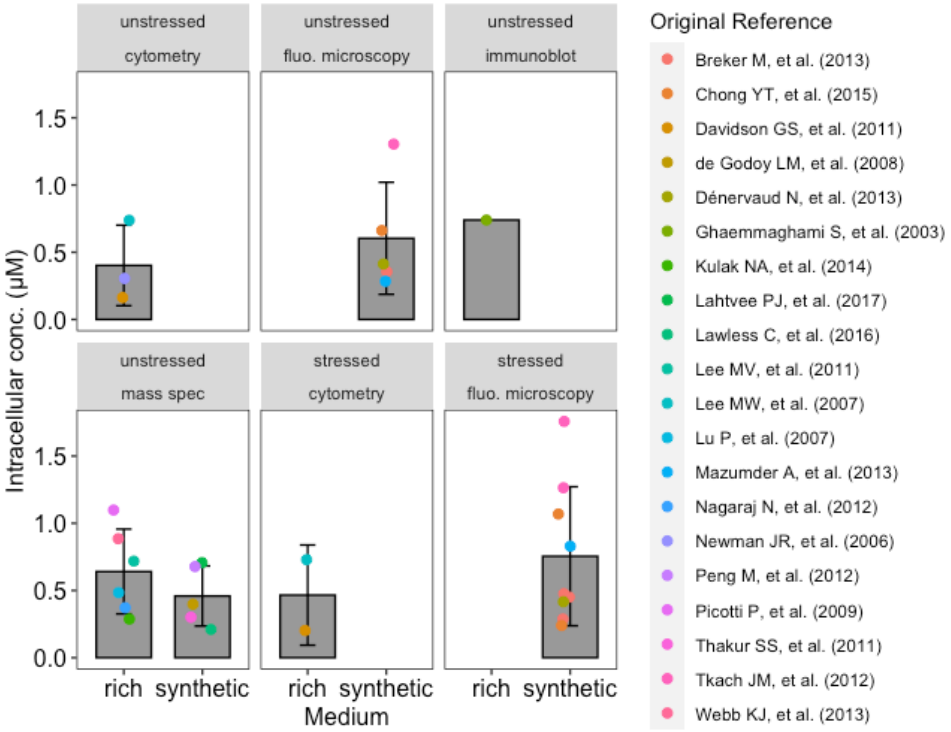

Figure 7: Purine nucleotides attenuate the assembly of the Ade4 particles *in vitro*

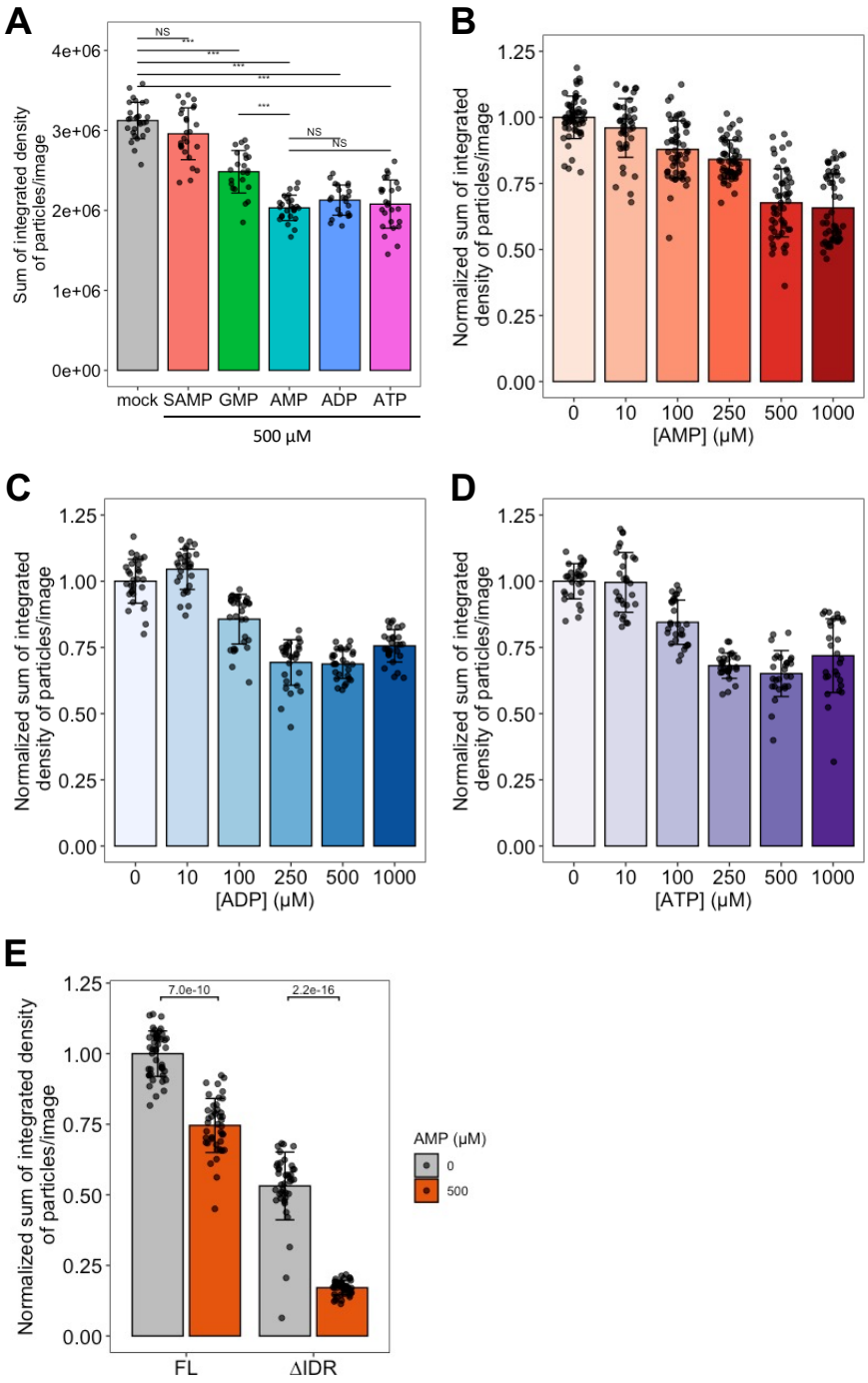

F

Condition 1:
Cytoplasmic macromolecular crowding

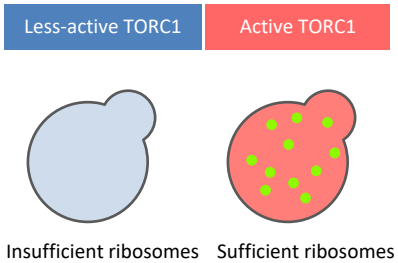

Condition 2:
Inhibitory interaction with purine nucleotides

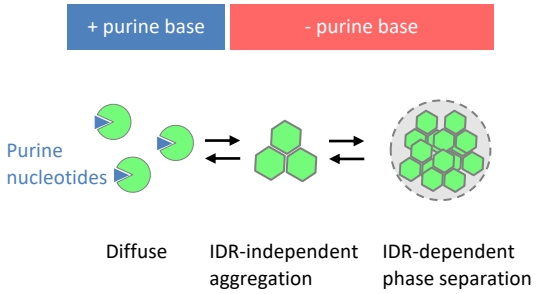

Figure 7S1: Additional data regarding the assembly of the Ade4 particles *in vitro*, related to Fig. 7

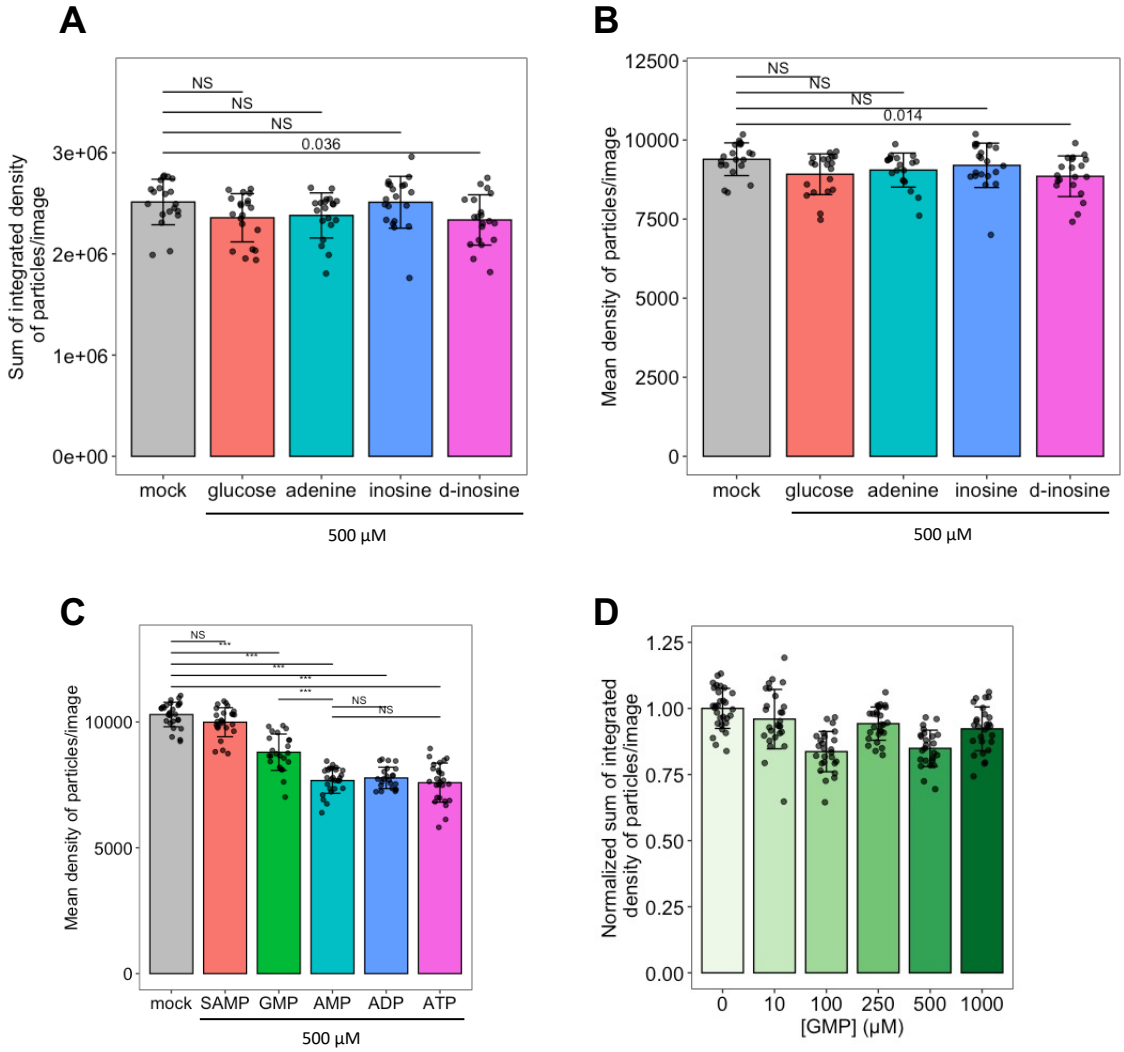

Figure 8: The formation of the Ade4 granules is important for efficient *de novo* purine synthesis during cell growth

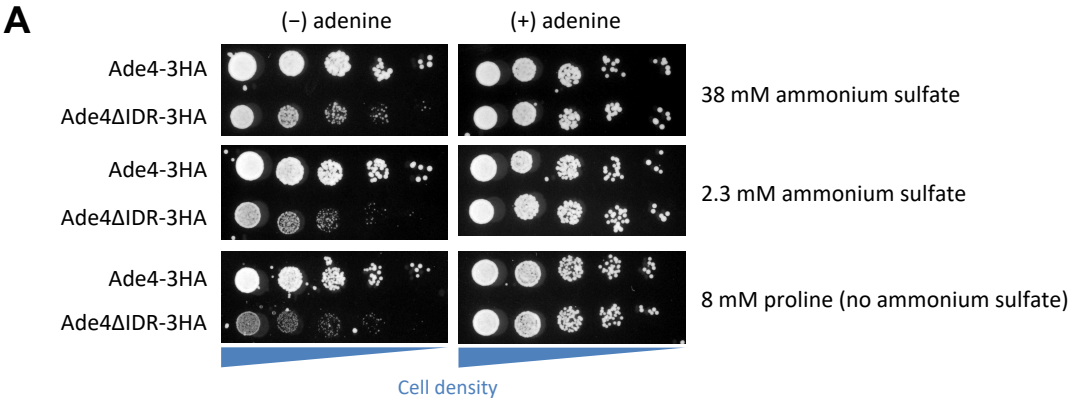

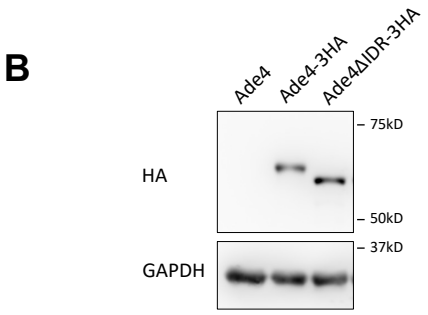

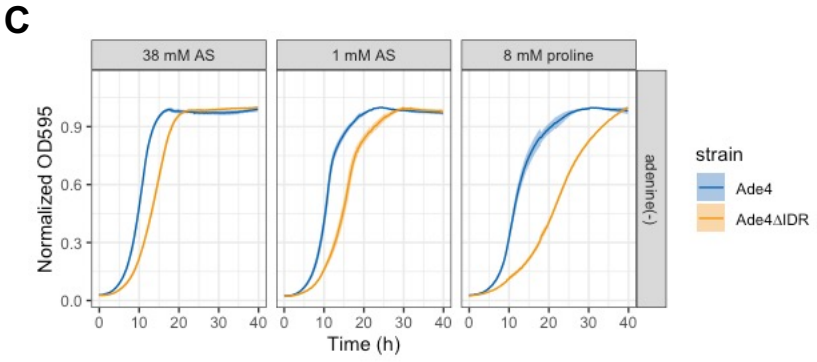

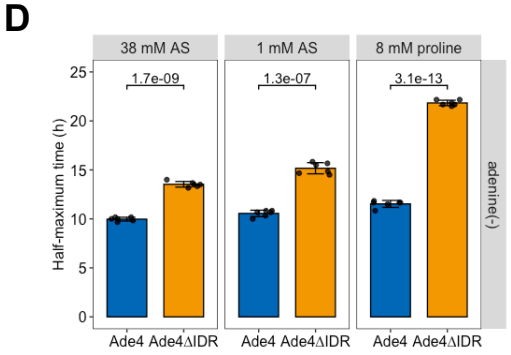

Figure 8S1: Cell growth assay in the presence of external purine bases , related to Fig. 8

A

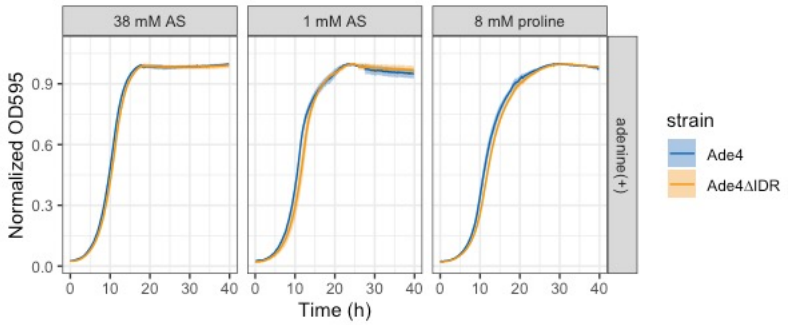

B

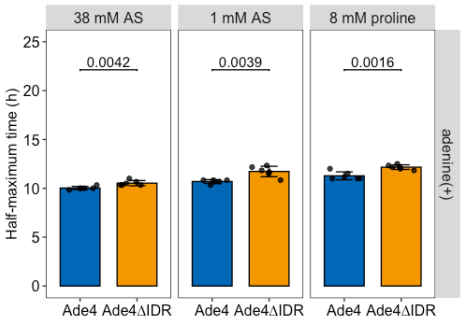

C

Gln-PRA activity:
PRPP + Gln + H_2O → PRA + Glu + PP_i

NH_3-PRA activity:
PRPP + NH_3 → PRA + PP_i

D

	Gln-PRA	NH_3-PRA
Low NH_3	Up	Down
High NH_3	Down	Up

Figure 9: MD calculations predict the potential leakage of glutamine-derived NH_3 from PPAT molecules

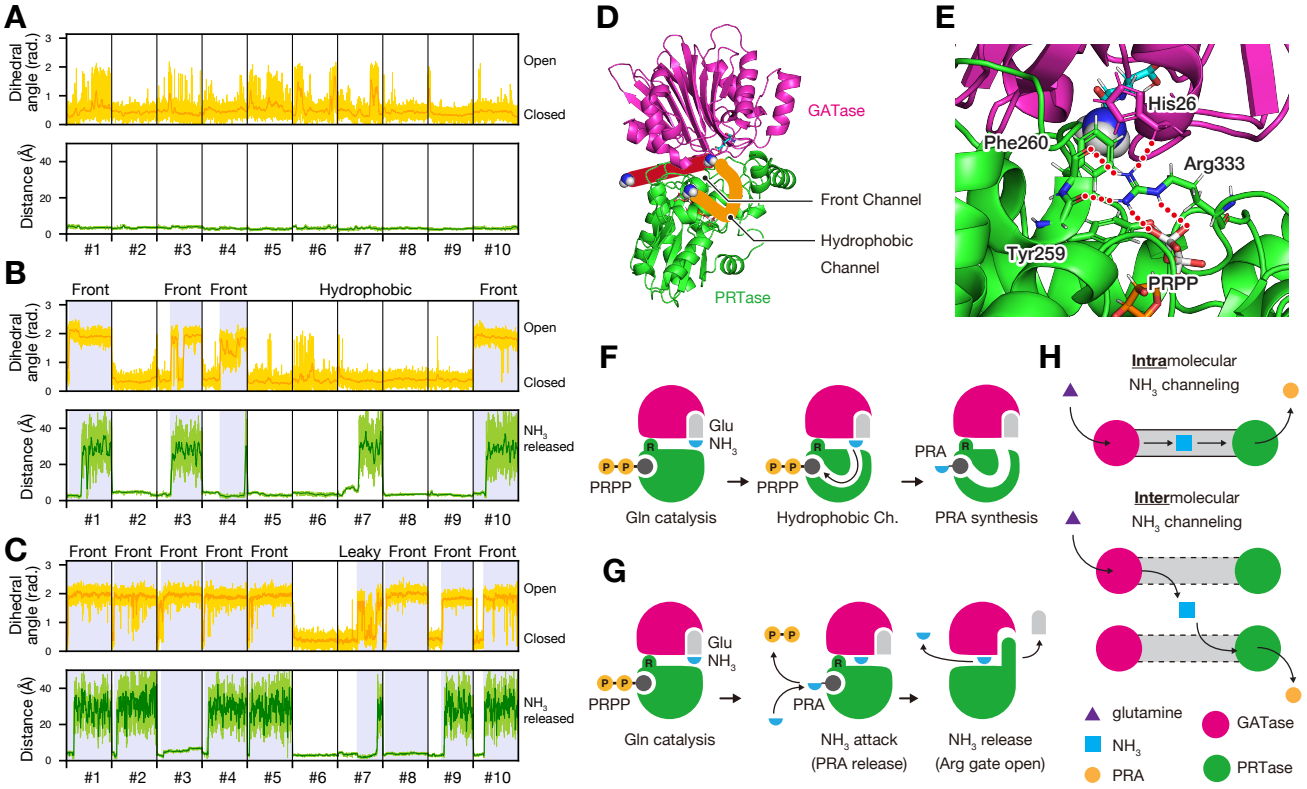
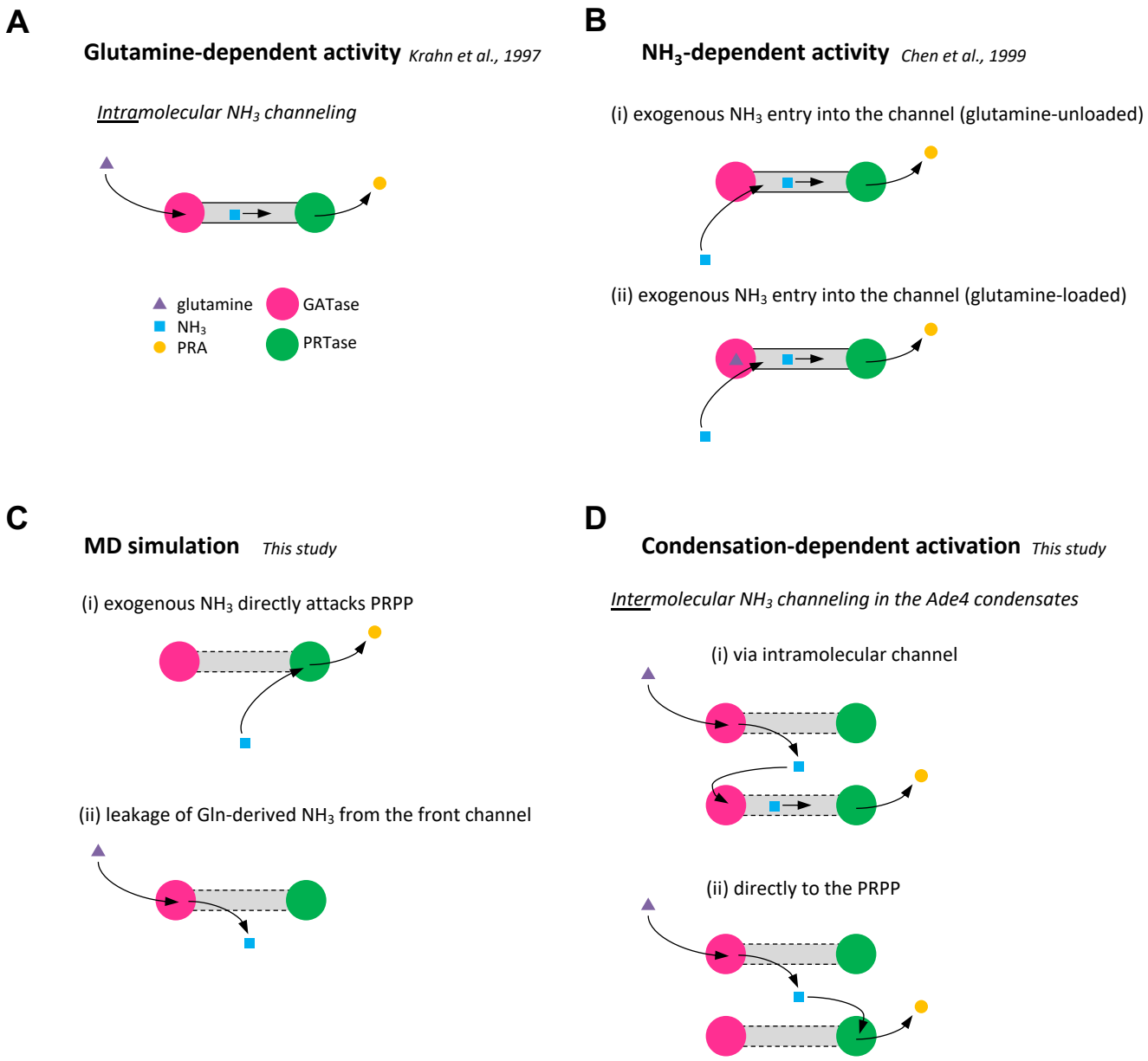
Figure 9S1: Possible enzymatic reaction pathway of PPAT